Dynamics regularization with tree-like structures

Rochelle Nieuwenhuis[a], Madoka Kubota[b], M. R. Flynn[c], Masayuki Kimura[d], Takashi Hikihara[d], Vakhtang Putkaradze[a,*]

[a] *Department of Mathematical and Statistical Sciences, University of Alberta Edmonton, AB, T6G 2G1 Canada*
[b] *Fuji Electric, Power Electronics Technology Development Center, Product Technology Laboratory, 1, Fuji-machi, Hino-city, Tokyo 191-8502, Japan*
[c] *Department of Mechanical Engineering, University of Alberta, Edmonton, AB, T6G 2G8 Canada*
[d] *Department of Electrical Engineering, Kyoto University, Katsura, Kyoto, 615-8510, Japan*

Abstract

The dynamics of a fully nonlinear, tree-structured resonator and its response to a broadband forcing of the branches is examined. It is shown that the broadband forcing yields a transfer of energy between the parts of the spectrum so that the spectrum becomes progressively more narrow-band for each level of the tree-like structure in the direction of the stem. We show that this behavior is in contrast to the response of a linear oscillator, which simply filters out the harmonics away from the resonance. We term such behaviour "regularization" and examine its significance for two- and three-dimensional motion using a Lagrangian framework. Key to our analysis is to investigate the dependence of the spectrum of motion, and its narrowing, on the parameters of the tree-like structure, for instance the lengths of different branches. Model predictions are obtained for idealized wind forcing characterized by an airflow that is interrupted at random time intervals. Our numerically-derived results are then compared against the data collected from select analogue laboratory experiments, which confirm the robust nature of the vibration regularization.

Keywords:
Nonlinear dynamics, Coupled nonlinear oscillators, Tree-like structures, Dynamics regularization

*Corresponding author
Email address: putkarad@ualberta.ca (Vakhtang Putkaradze)

1. Introduction and literature review

The dynamics of connected non-linear resonators has played an important role in both fundamental science and engineering [1]. On the application side, the question of the response of such systems to strongly non-harmonic or non-constant forcing has been one of the main inspirations driving the development of the field. The case of energy absorption from incoherent, random forces is known more generally as *broadband harvesting* [2]. Mechanical devices constructed for the purpose of utilizing broadband sources are normally based on a set of moveable objects positioned on a flexible piezoelectric element [3]; they convert the motion of the underlying substrate (*e.g.* vibration) into the deformation of a piezo element and thereby produce energy. The efficiency and power output of these devices depends to a large extent on the nature of motion of the power-generating element, as well as other factors. Piezo-electric devices achieve the highest efficiency when they operate within an optimal frequency band, and the efficiency drops rapidly outside this band [4, 5, 6, 7, 8]. To focus the ambient forcing into the motion of the resonator in the optimal frequency band, strong nonlinearity, bi-stability and chaotic responses remain topics of active investigation [9, 10, 11, 12, 13, 14, 15, 16, 17, 18]. For larger devices, electromagnetic induction has been used to harvest narrow-band random excitation by exploiting highly nonlinear resonances [19, 20]. Recent work related to *vibro-wind* energy generation explores the combined dynamics of a chain of such harvesters due to fluid-structure interactions [21], the oscillations induced by vortex shedding behind arrays of flexible structures [22] and increased energy absorption from coupled Duffing oscillators [23].

In this paper, we show that it is possible to narrow the spectrum of broadband forcing using the nonlinear dynamics associated with coupled resonators arranged in a tree-like configurations. We focus on the dynamics of tree-like structures as a response to broadband forcing leaving the precise application of these ideas to energy harvesting to future works. We demonstrate that under quite general conditions, a broadband forcing applied to the top branches regularizes towards the stem, *i.e.*, the stem shows substantially more regular motion with a narrow bandwidth of the spectrum. In terms of spectral analysis of the signal for each level of the tree-like structure, such an effect would move energy between harmonics, mostly from the higher harmonics to the lower ones, making the spectrum more concentrated around a certain frequency. We show that this phenomenon comes from nonlinear effects, and is in contrast to Q1

a linear resonator, which acts as a filter centered around a certain frequency. Intuitively, this can be formulated as follows. Suppose, for simplicity, that we consider a completely white spectrum absorbed by the device. This is illustrated in Figure 1 by the flat line and a sample of harmonics with given amplitude, shown as arrows. For each frequency, a linear filter like a resonating linear oscillator will simply multiply the amplitude of the spectrum of the harmonics by a certain function. On the other hand, re-arrangement of the modes, which is a purely nonlinear effect, will reposition the location of the harmonics, centering the sampled arrows around a given frequency (or perhaps several frequencies), thus making the spectral density higher at this point. These are fundamentally different concepts, as can be seen from the Figure 1. In reality, both effects will be present in any realistic system. Regularization having nonlinear effects as a leading cause of band-narrowing will preserve much more of the high harmonic content than a typical linear filter.

Formally, we define band-narrowing as the transformation of a signal when more power in the spectrum is moved to lower bandwidths and concentrated about a single frequency. While this definition is somewhat inexact, we note that a precise mathematical definition of this notion, applicable to a broad range of physical cases, appears elusive. An important consequence of our approach is that the band-narrowing, or regularization, is achieved due to the structure of the system itself, without requiring external control mechanisms.

Although the associated quantitative details will be shown to be nontrivial, the conceptual foundation is simple. Consider, for instance, a tree swaying in the wind. Whereas the movement of the trunk is typically quite regular, the motion of the branches is much less so. Unfortunately, energy extraction from real trees is difficult: recent investigations [24, 25] of life-sized trees yielded quite modest power generation, *i.e.* 44 mW from the trunk and several Watts for the motion of entire (several meter tall) tree including the top branches. This rather disappointing result follows from the comparatively small deviations of the tree trunk from its equilibrium position, an evolutionary adaption presumably meant to minimize the likelihood of trunk fracture during violent wind storms. We therefore aim to construct artificial tree-like structures with characteristics that are in some sense opposite to real trees, providing potentially large amplitude displacements and an efficient regularization of the forcing.

In this paper, we use the term "trees" in the generalized sense, both for structures possessing a branched structure analogous to real trees and, alter-

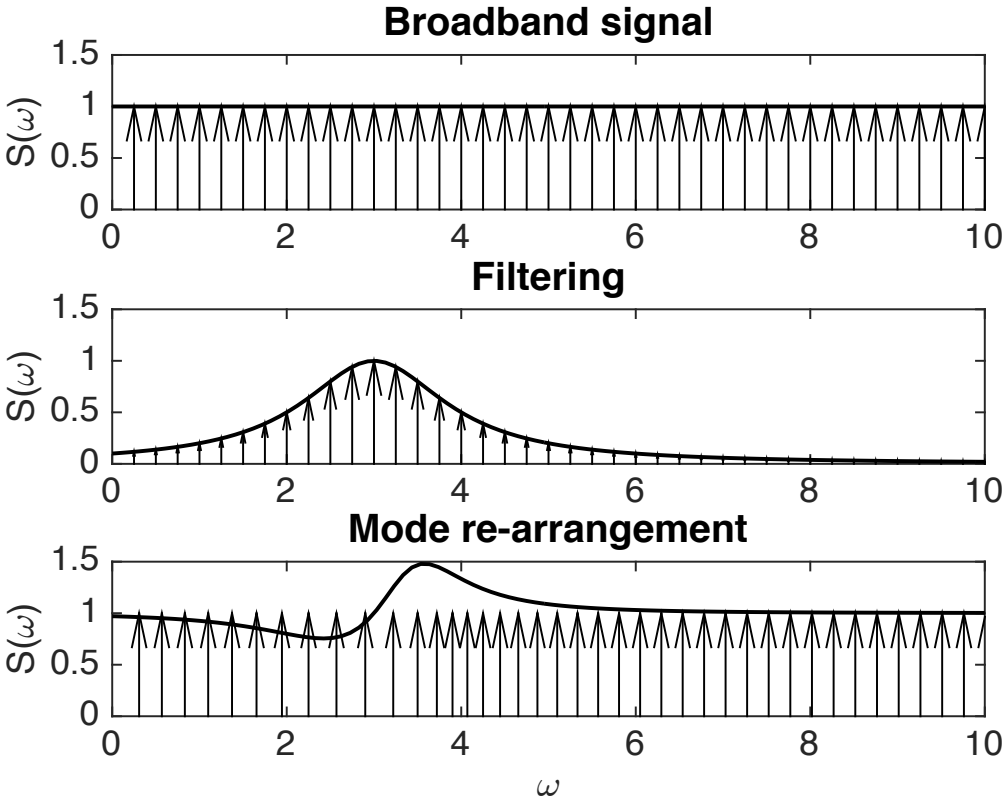

Figure 1: A schematic illustration of linear filtering vs regularization. A filter applied to an initially broadband signal with a flat spectrum will multiply the amplitude of each harmonic with the frequency response function. On the other hand, regularization re-shuffles the position on the harmonics making them more dense in some areas, thereby increasing the spectral density amplitude in these same areas.

natively, for coupled sequences of oscillators that exhibit a tree-like dynamical diagram. The former type is more useful for large-scale, low-frequency harvesting *e.g.* by wind or waves whereas the latter is more relevant for miniaturized harvesting devices. Of course, a multi-level structure exhibiting branching has many resonances and thus increased response to broadband forcing. In fact, our design should be understood as the next step from devices with internal resonating structures [26], such as sequentially connected nonlinear oscillators which were recently suggested as an effective tool for energy harvesting [27]. In our case, the regularization of the vibration at each level relies on an interaction of nonlinearity and multiple coupled resonances and cannot be explained solely by a linear analysis.

The rest of the paper is organized as follows. Section 2 discusses the mechanics of tree-like structures, from the theoretical foundation to laboratory experiments. Section 3 outlines theoretical explanations of observed results in terms of a broadening of the nonlinear amplitude response. Finally in Section 4, we present conclusions and outline future directions for applications using tree-like structures.

2. Flexible tree-like structures – theory and laboratory experiment

In this section, we shall study the flexible tree-like structure exhibited schematically in Figure 2 a. Two scenarios are considered, namely deformations in the $x-y$ plane shown in Figure 2 b, and deformations normal to the $x-y$ plane, shown in Figure 3 and considered in Sec. 2.2. Note that the case of static bifurcation was examined in detail in [28], where each branch was also considered as an elastic rod. We present the results of a static bifurcation analysis, being inevitably much simpler than the one undertaken in [28], in Appendix A. For the sake of analytical tractability, we only consider the compliance at the joints connecting rigid branches. Hache *et al.* [29] present further details of such models and the application of discrete-to-continuum approaches to the vibration and stability of beams. A more general scenario can be examined by adapting the extended theory developed in [28]. This latter approach requires solving PDEs at each branch, and will be investigated in future studies. In our simplification, limiting the dynamics to a bending of the joints only, the branches' deformation is modelled through the motion of rigid rods connected by nonlinear springs at the joints. Our planar model described in Sec. 2.1, as well as the planar mass-spring models considered in Appendix B, are quite similar to the models of tree dynamics and their spring-mass equiv- Q5

alents derived in [30] from Newtonian mechanics. The three-dimensional model developed in Sec. 2.2 is, as far as we know, novel. In addition we note that our paper focuses on dynamics regularization, *i.e.* the increase of regularity of the spectrum of the motion from the outer branches to the stem. In what follows, we shall start with the case where the deformation of the tree is limited to the plane of the tree itself. These dynamics are relevant *e.g.* to the tilting of the base of a tree-like structure with a deformation that has a broadband spectrum, such as a tree structure on a platform that is forced by ocean waves. We shall defer the experimental study of such systems to the future, and will instead use the analytical model of Sec. 2.1 to serve as a pedagogical introduction to the more complex system of 3D dynamics described in Sec. 2.2. An understanding of these 3D dynamics is essential because of the inherent difficulty of constraining real motions to a plane, particularly for the irregular forcing that characterizes the energy-harvesting applications relevant to the ideas presented in this work. In both Sec. 2.1 and Sec. 2.2, Q6
and so as to avoid problems of unwieldy complexity, we terminate the branching after level 2. The general dynamics of n-branched systems has been derived in other contexts, e.g. Gay-Balmaz et al. [31] examined the dynamics of branched polymers and included in their analysis a description of Poisson brackets and conservation laws. For a general n-level system, the description in terms of abstract symmetry-reduced variables is possible, but the actual implementation as a system of coupled ODEs is too cumbersome to provide any analytical insight.

2.1. Two dimensional planar oscillations: theory

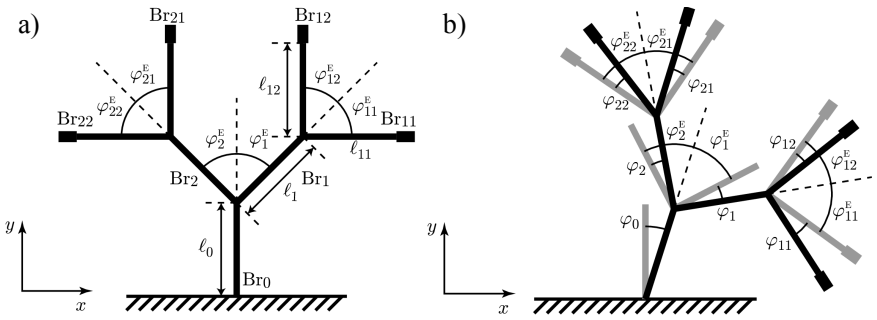

Figure 2: A schematic and definition of variables for a tree-like structure viewed from the front. Panel a) - undisturbed configuration defining equilibrium angles. Panel b) - deformed configuration in the plane defining notations for local angles.

Our analysis begins with the computation of the corresponding Lagrangian. We denote each level using index notation, with the lowest order or base level (stem) having index 0, the next level having index i and the following level having index ij. We use the notation φ for the relative angles of the branches, and Φ for the absolute angles with respect to a fixed (vertical) axis. This reflects the fact that the equilibrium position of a branch is in general inclined with respect to the vertical axis; superscript E is used to denote the equilibrium value of the angle in question. In this notation, the vector $\mathbf{c}$ connecting the nearest pivot point of each branch towards the stem to the branch centre of mass for a given configuration is

$$\mathbf{c}_0 = \frac{\ell_0}{2}\left(\sin(\varphi_0 + \Phi_0^{\mathrm{E}}),\ \cos(\varphi_0 + \Phi_0^{\mathrm{E}})\right), \tag{1}$$

$$\mathbf{c}_i = \frac{\ell_i}{2}\left(\sin(\varphi_i + \varphi_0 + \Phi_i^{\mathrm{E}}),\ \cos(\varphi_i + \varphi_0 + \Phi_i^{\mathrm{E}})\right), \tag{2}$$

$$\mathbf{c}_{ij} = \frac{\ell_{ij}}{2}\left(\sin(\varphi_{ij} + \varphi_i + \varphi_0 + \Phi_{ij}^{\mathrm{E}}),\ \cos(\varphi_{ij} + \varphi_i + \varphi_0 + \Phi_{ij}^{\mathrm{E}})\right), \tag{3}$$

where $\Phi_0^{\mathrm{E}}\,(=\varphi_0^{\mathrm{E}})$, $\Phi_i^{\mathrm{E}}\,(=\varphi_0^{\mathrm{E}}+\varphi_i^{\mathrm{E}})$, $\Phi_{ij}^{\mathrm{E}}\,(=\varphi_0^{\mathrm{E}}+\varphi_i^{\mathrm{E}}+\varphi_{ij}^{\mathrm{E}})$ are the mounting angles of each branch and ℓ_0, ℓ_i, ℓ_{ij}, φ_i^{E} and $\varphi_{ij}^{\mathrm{E}}$ are defined in Figure 2. From equations (1–3), the coordinate of the centre of mass of each branch is given by

$$\mathbf{r}_0 = \mathbf{c}_0\,, \quad \mathbf{r}_i = 2\mathbf{c}_0 + \mathbf{c}_i\,, \quad \mathbf{r}_{ij} = 2\mathbf{c}_0 + 2\mathbf{c}_i + \mathbf{c}_{ij}\,, \quad \mathbf{r}_{ij}^{\mathrm{W}} = 2\mathbf{c}_0 + 2\mathbf{c}_i + 2\mathbf{c}_{ij}\,, \tag{4}$$

where $\mathbf{r}_{ij}^{\mathrm{W}}$ denotes the position of a weight attached to the top of branch B_{ij}. The centre of mass of each branch moves with a velocity computed by differentiating (4), *i.e.* $\mathbf{v}_\bullet = \dot{\mathbf{r}}_\bullet$, where "$_\bullet$" stands for any one of "$_0$", "$_i$", "$_{ij}$" or "$^{\mathrm{W}}_{ij}$". Using the equation for the moment of inertia with respect to the centre of mass of a beam ($I = m\ell^2/12$ where m is the mass), the expression for the kinetic energy K is:

$$\begin{aligned} K =& \frac{1}{2}\left(m_0|\mathbf{v}_0|^2 + \frac{m_0\ell_0^2}{12}\dot{\varphi}_0^2\right) + \frac{1}{2}\sum_i m_i|\mathbf{v}_i|^2 + \frac{m_i\ell_i^2}{12}\left(\dot{\varphi}_0 + \dot{\varphi}_i\right)^2 \\ &+ \frac{1}{2}\sum_{i,j} m_{ij}|\mathbf{v}_{ij}|^2 + \frac{m_{ij}\ell_{ij}^2}{12}\left(\dot{\varphi}_0 + \dot{\varphi}_i + \dot{\varphi}_{ij}\right)^2 + \frac{1}{2}\sum_{i,j} m_{ij}^{\mathrm{W}}\left|\mathbf{v}_{ij}^{\mathrm{W}}\right|^2. \end{aligned} \tag{5}$$

The corresponding results for the potential energy of deformation (P_b) and

gravity (P_g) read

$$P_b = \frac{1}{2}\alpha_0\varphi_0^2 + \frac{1}{4}\beta_0\varphi_0^4 + \sum_i \left(\frac{1}{2}\alpha_i\varphi_i^2 + \frac{1}{4}\beta_i\varphi_i^4\right) + \sum_{i,j}\left(\frac{1}{2}\alpha_{ij}\varphi_{ij}^2 + \frac{1}{4}\beta_{ij}\varphi_{ij}^4\right), \quad (6)$$

$$P_g = m_0 g r_{0,y} + \sum_i (m_i g r_{i,y}) + \sum_{i,j}(m_{ij} g r_{ij,y}) + \sum_{i,j}\left(m_{ij}^{\mathrm{W}} g r_{ij,y}^{\mathrm{W}}\right), \quad (7)$$

respectively, where $r_{\bullet,y}$ represents the vertical-component of the position vector $\mathbf{r}_\bullet$, and g is gravitational acceleration assumed to point downwards in the y-direction. The coefficients $\alpha_\bullet$ and $\beta_\bullet$ represent, correspondingly, the linear and nonlinear elasticity parameters. We have used a simple one degree of freedom, nonlinear model of the beam deformation describing all the energy of the deformed beam in terms of a characteristic deformation angle $\varphi_\bullet$. Here, the 4th order nonlinearity in the angles models the nonlinear response of the joints, which we have chosen to be symmetric with respect to $\varphi_\bullet \to -\varphi_\bullet$. This nonlinearity arises both as a model of nonlinear beam deflection and also nonlinearity of the joint, see, *e.g.,* [30]. This model, at least mathematically, is equivalent to a nonlinear oscillator with a single degree of freedom. Using the Lagrangian $\mathcal{L} = K - P_b - P_g - P_e$, including the potential of the applied external force P_e, as well as a Rayleigh dissipation function $\mathcal{F}$ incorporating a viscous friction-like term, the final equations of motion for branch $\bullet$ are given by the Euler-Lagrange equations Q7

$$\frac{\mathrm{d}}{\mathrm{d}t}\frac{\partial \mathcal{L}}{\partial \dot{\varphi}_\bullet} - \frac{\partial \mathcal{L}}{\partial \varphi_\bullet} + \frac{\partial \mathcal{F}}{\partial \dot{\varphi}_\bullet} = f_\bullet\,. \quad (8)$$

Here, we have also introduced, for generality, a non-conservative generalized forcing with the component $f_\bullet$ acting on the branch with the index $\bullet$. In our modeling approach, the non-conservative contribution of the force is absent, as the forcing of the wind in its simplest approximation is assumed to be constant. However, more complex models of the wind motion may include non-conservative forcing. We have chosen to compute the external force coming from the external potential P_e, for the sake of simplicity of computation of the generalized forces. Consideration of more complex forces, *i.e.*, non-potential forces is possible, but we shall not consider them here as it will render the computation of the generalized external force on each branch cumbersome. To model the applied external force from *e.g.* wind or other

sources, we introduce the time-varying forcing function $F_{\text{ext}}(t)$, acting in the direction x and constant in space, common for all branches and corresponding to a dimensionless force per unit area. Thus, assuming that at each point in time, the potential energy is constant in space, we define the potential energy of the external force as [32] Q8

$$P_e = A_0 F_{\text{ext}}(t) r_{0,x} + \sum_i \left(A_i F_{\text{ext}}(t) r_{i,x}\right) + \sum_{i,j} \left(A_{ij} F_{\text{ext}}(t) r_{ij,x}\right) + \sum_{i,j} \left(A^{\text{W}}_{ij} F_{\text{ext}}(t) r^{\text{W}}_{ij,x}\right). \tag{9}$$

Here, $A_\bullet$ denotes the area of the branch exposed to the external wind $F_{\text{ext}}(t)$, with $r_{\bullet,x}$ being the cosine of the direction of the wind and the normal to the branch, assumed to be flat. The superscript W denotes the additional force on the 'leaves' of the tree. Q8 The generalized forces are then computed as derivatives of P_e with respect to the corresponding angles $\varphi_\bullet$. We take damping to be proportional to the time derivative of the position $\mathbf{v}_\bullet$ with a proportionality factor $\gamma_\bullet$. Therefore, the Rayleigh dissipation function can be written as

$$\mathcal{F} = \frac{1}{2}\gamma_0 |\mathbf{v}_0|^2 + \frac{1}{2}\sum_i \gamma_i |\mathbf{v}_i|^2 + \frac{1}{2}\sum_{i,j} \gamma_{ij} |\mathbf{v}|^2_{ij} + \frac{1}{2}\sum_{i,j} \gamma^{\text{W}}_{ij} \left|\mathbf{v}^{\text{W}}_{ij}\right|^2. \tag{10}$$

We note that Raleigh's dissipation function models the effect of viscous-like friction of a particular type coming either from other the ambient media, or internal friction inside the joints. More complex models for the friction can be considered, which we will postpone for further studies. Q18 From (10), one then needs to express the velocities in terms of the derivatives of angles, and to differentiate in (8). To avoid undue algebraic complexity, (8) is not presented in expanded form.

2.2. Three dimensional normal oscillations: theory

We now turn our attention to the more experimentally and practically relevant case presented in Figure 3, where the undisturbed tree position is in the plane normal to the direction of the external force. Indeed, in the experiments to be discussed below, the wind bends the tree in a direction normal to the plane of the equilibrium position. Although the chaotic nature of a real turbulent flow makes it impossible to make a precise quantitative comparison between theory and experiment, it is nonetheless helpful to use a

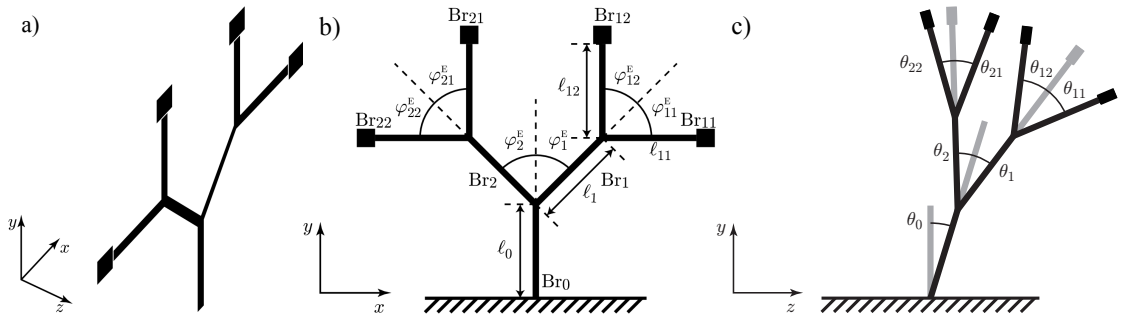

Figure 3: Tree-like structure oscillating normal to the $x-y$ plane. Panel a): undisturbed configuration, three-dimensional view. Panel b): undisturbed configuration, front view. panel c): deformed configuration, side view.

model that is capable of describing physically precise 3D dynamics. In Figure 3, $\varphi^{\mathrm{E}}_{\bullet}$ represents the mounting angles of each branch, which are assumed to be fixed. Each branch will rotate with angle $\theta_{\bullet}$. Using the notation $\bullet$ introduced before for subscripts "$_0$", "$_i$" or "$_{ij}$", it is convenient to define the initial ('ini') position vectors of each branch having index $\bullet$ as

$$\mathbf{r}_{\bullet,\mathrm{ini}} = \frac{1}{2}\ell_{\bullet}\mathbf{R}_z(\Phi^{\mathrm{E}}_{\bullet})\mathbf{e}_y, \tag{11}$$

where $\mathbf{e}_y$ is the unit vector $(0,1,0)^T$ and $\mathbf{R}_z(\theta)$ is a rotation matrix around the z-axis with an angle θ. The difference from the two-dimensional planar oscillations is that each branch now rotates around one fixed axis, which is taken to be the x-axis describing the tilt. Here, for the sake of simplicity, we assume that each branch only rotates about the fixed axis and is thus characterized by one angle of rotation only. For general motions, the rotation matrix will be characterized by three parameters, such as Euler angles, and both the equations of motion and their analysis will be considerably more complex – see Appendix C and [31]. In light of the above, the normal to branch $\bullet$ is described as

$$\hat{\mathbf{n}}_{\bullet} = \mathbf{R}_x(\Phi^{\mathrm{E}}_{\bullet})\mathbf{e}_x\,, \tag{12}$$

where $\mathbf{e}_x = (1,0,0)^T$. Rotation matrices around the z-axis are given by

$$\mathbf{R}_{\hat{\mathbf{n}}_\bullet}(\theta_\bullet) = \hat{\mathbf{n}}_\bullet \otimes \hat{\mathbf{n}}_\bullet + (\mathrm{Id}_{3\times 3} - \hat{\mathbf{n}}_\bullet \otimes \hat{\mathbf{n}}_\bullet)\cos\theta_\bullet + \mathbf{S}_\bullet \sin\theta_\bullet \tag{13}$$

$$\mathbf{S}_\bullet = \begin{pmatrix} 0 & \hat{n}_{\bullet,z} & -\hat{n}_{\bullet,y} \\ -\hat{n}_{\bullet,z} & 0 & \hat{n}_{\bullet,x} \\ \hat{n}_{\bullet,y} & -\hat{n}_{\bullet,x} & 0 \end{pmatrix}, \quad \mathrm{Id}_{3\times 3} = \begin{pmatrix} 1 & 0 & 0 \\ 0 & 1 & 0 \\ 0 & 0 & 1 \end{pmatrix}, \tag{14}$$

$$\hat{\mathbf{n}}_\bullet \otimes \hat{\mathbf{n}}_\bullet = \begin{pmatrix} \hat{n}^2_{\bullet,x} & \hat{n}_{\bullet,x}\hat{n}_{\bullet,y} & \hat{n}_{\bullet,x}\hat{n}_{\bullet,z} \\ \hat{n}_{\bullet,x}\hat{n}_{\bullet,y} & \hat{n}^2_{\bullet,y} & \hat{n}_{\bullet,y}\hat{n}_{\bullet,z} \\ \hat{n}_{\bullet,x}\hat{n}_{\bullet,z} & \hat{n}_{\bullet,y}\hat{n}_{\bullet,z} & \hat{n}^2_{\bullet,z} \end{pmatrix}. \tag{15}$$

The positions of each branch are thus obtained from (11) and (15) as

$$\mathbf{r}_0 = \mathbf{R}_{\hat{\mathbf{n}}_0}(\theta_0)\mathbf{r}_{0,\mathrm{ini}}\,, \tag{16}$$

$$\mathbf{r}_i = \mathbf{R}_{\hat{\mathbf{n}}_0}(\theta_0)\left(\mathbf{R}_{\hat{\mathbf{n}}_i}(\theta_i)\mathbf{r}_{i,\mathrm{ini}} + 2\mathbf{r}_{0,\mathrm{ini}}\right), \tag{17}$$

$$\mathbf{r}_{ij} = \mathbf{R}_{\hat{\mathbf{n}}_0}(\theta_0)\left\{\mathbf{R}_{\hat{\mathbf{n}}_i}(\theta_i)\left(\mathbf{R}_{\hat{\mathbf{n}}_{ij}}(\theta_{ij})\mathbf{r}_{ij,\mathrm{ini}} + 2\mathbf{r}_{i,\mathrm{ini}}\right) + 2\mathbf{r}_{0,\mathrm{ini}}\right\}, \tag{18}$$

$$\mathbf{r}^{\mathrm{W}}_{ij} = \mathbf{R}_{\hat{\mathbf{n}}_0}(\theta_0)\left\{\mathbf{R}_{\hat{\mathbf{n}}_i}(\theta_i)\left(\mathbf{R}_{\hat{\mathbf{n}}_{ij}}(\theta_{ij})2\mathbf{r}_{ij,\mathrm{ini}} + 2\mathbf{r}_{i,\mathrm{ini}}\right) + 2\mathbf{r}_{0,\mathrm{ini}}\right\}. \tag{19}$$

The kinetic and potential energies associated with oscillations normal to the $x-y$ plane are derived by replacing $\varphi_\bullet$ by $\theta_\bullet$ in (5-7), and by providing an appropriate generalization of the potential for the external force P_e. The Euler-Lagrange equations utilize the Lagrangian $\mathcal{L} = K - P_b - P_g - P_e$, and Rayleigh's dissipation function $\mathcal{F}$ for damping, giving equations of motion

$$\frac{\mathrm{d}}{\mathrm{d}t}\frac{\partial \mathcal{L}}{\partial \dot{\theta}_\bullet} - \frac{\partial \mathcal{L}}{\partial \theta_\bullet} + \frac{\partial \mathcal{F}}{\partial \dot{\theta}_\bullet} = f_\bullet. \tag{20}$$

Here, similar to (8), we have introduced the generalized non-conservative forcing $f_\bullet$ acting on branch $\bullet$. As in equation (8), this non-conservative forcing term is absent in the subsequent theoretical discussion due to the basic approximation about the wind forcing used, with the external forcing entering the Lagrangian through an appropriately defined potential energy term. Again, for reasons of algebraic complexity, these equations are not presented in their expanded form – see Appendix C for more details.

2.3. Numerical simulations and analysis of dynamics

Whereas the spectral structure of a real turbulent flow is highly complex, here we limit our attention to a broadband wind forcing defined by

$$F_{\mathrm{ext}}(t) = G \star f(t)\,, \quad f(t) = \begin{cases} 0, & t_{2k} < t < t_{2k+1} \\ N, & t_{2k+1} \le t < t_{2k+2} \end{cases} \tag{21}$$

i.e., we assume a convolution of a smoothing kernel $G(t)$ with a step-like function jumping from 0 to N at random intervals. More precisely, define a function $f(t)$ in the following way. Take t_n is the sequence of strictly increasing positive numbers, such that on every interval starting with an even index $t_{2k} < t < t_{2k+1}$, $f(t)$ vanishes, and on every interval starting with an odd index $t_{2k+1} < t < t_{2k+2}$, $f(t)$ is equal to some fixed strength (amplitude) N. Then, the forcing on the tree $F_{\text{ext}}(t)$ is equal to the convolution of a smoothing kernel with the function $f(t)$. The kernel $G(t)$ is normalized so that $\int_{-\infty}^{+\infty} G(t)\mathrm{d}t = 1$. The randomness of the forcing is enforced by requiring that the length of the time intervals defining no forcing $t_{2k} < t < t_{2k+1}$ and constant forcing $t_{2k+1} \leq t < t_{2k+2}$ take on random values with a prescribed distribution. Although an exact comparison cannot be made between numerical simulations and laboratory measurements, this type of forcing is chosen to broadly mimic the experimental setup presented in Sec. 2.4 below, where a wind of constant velocity is interrupted at random time intervals. In particular, the convolution with a localized function $G(t)$ acts as a filter smoothing the jump transition in the forcing and taking into account the time necessary to open and close the wind barrier in our experimental wind tunnel. Our studies indicate that the exact nature of the smoothing function $G(t)$ is not essential for the low-frequency behavior of the branches. Experimentally, such type of wind presents the simplest way of generating an external forcing rich in high order harmonics on scales comparable to the temporal scales of the tree-like structure. On the other hand, a function with a discontinuity at $t = t_k$ possesses a strongly broadband spectrum, with the n-th Fourier harmonic decaying as $1/n$ in the limit $n \to \infty$. The convolution with the function $G(t)$ in (21) enforces sufficiently rapid harmonic decay beyond a certain threshold. We present our results for the choice of the convolution function

Q8

$$G(t) = \frac{1}{2\Delta T} \begin{cases} 1, & |t| < \Delta T \\ 0, & |t| > \Delta T \end{cases} \tag{22}$$

Other choices of the convolution kernel $G(t)$, for example, a Gaussian kernel, alter the details of the forcing function behavior in the higher harmonics, but seemingly do not play a role in the low-frequency behavior of interest here. Thus, we believe that the forcing described by (21) has both a mathematical relevance insofar as possessing a broadband spectrum, and a physical significance insofar as being a model for gusty winds. While studying the behavior caused by broadband forces is of particular interest here, we also analyze the nonlinear response of the theoretical model to a single harmonic forcing, or

some combination of harmonics in Appendix B.2 and Sec. 3, respectively. However, such harmonic-like forcing is difficult to achieve in wind tunnel experiments, and the discussion of such forcing will be limited to model analysis only.

The external forces contained in (8) and (20) through the potential energy term (9) and its corresponding generalization for the 3D case are assumed to be applied to the centre of mass, coinciding with the geometric centre, of each branch. This is a reasonable approximation for wind forcing on a uniform plate positioned normal to the oncoming air flow. For more general configurations, this assumption should be understood as a first approximation only; however, we do not expect that the main results of this paper concerning band narrowing will change substantially if more complicated models of external forcing are employed. The parameters of the single degree of freedom nonlinear oscillators modelling the elastic beams are chosen to correspond to experimental values from the experiment described below in Sec. 2.4.

Numerical simulations of (8) and (20) were performed using *Mathematica*. The temporal variation for each successive level shows an increasing degree of irregularity, which can be quantified by considering the spectrum of the deviation from equilibrium. Results corresponding to the two-dimensional planar and normal motions described, respectively, by (8) and (20) are shown in Figures 4 a,b. In both cases there is the progressive emergence of a dominant spectral peak as the level index decreases or, equivalently, as the deviation from equilibrium is measured closer to the stem. Despite the highly irregular nature of the forcing, the motion of the stem is comparatively regular, as is evident from the spectral peak observed at low frequency, and much lower amplitudes of the higher harmonics at the stem compared to the branches. We have repeated the numerical experiments varying the ratio of the natural period (inverse of natural frequency) of individual branches to the time interval, taken to be 0.2 s in Figure 4, and the results are similar. As expected, the band-narrowing diminishes when the natural period of the individual branches exceeds the typical time interval of the forcing. Thus, for efficient band-narrowing, one needs to optimize the parameters of the tree mechanics to correspond to typical time scales of the forcing. Note that we use slightly different time scales in Figures 4 a,b in order to represent the most important features of both systems. Note also that the band-narrowing is most pronounced in the right panel of Figure 4, where the outer, middle and top branches experience oscillations with a frequency of about 4 Hz, connected to the resonant frequency of the branches as described above. That part of the spectrum is substantially

Q15

Q10

reduced in the stem, where most of the energy is shifted to the low frequencies. One could define the band-narrowing efficiency of the system depending on the removal of these high-frequency spectral components in the oscillations of the stem *e.g.* based on the areas under the curves for each branch level and for sufficiently large frequency. We shall quantify this intuitive concept later in Sec 3.

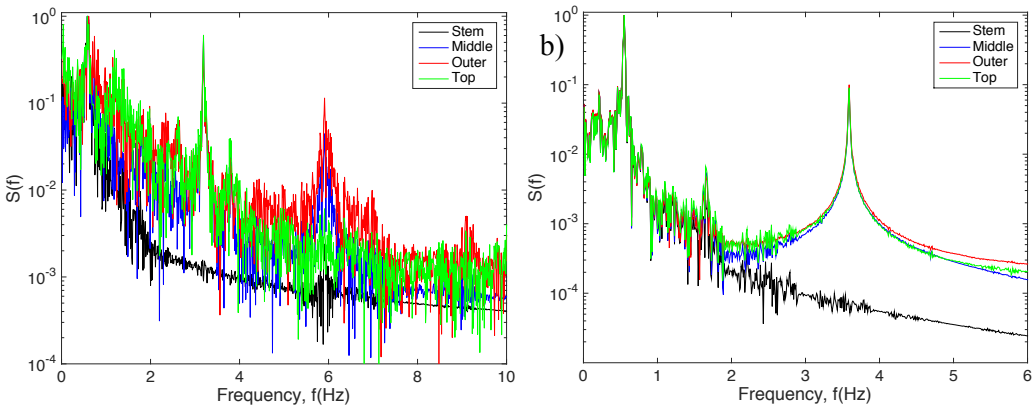

Figure 4: Normalized energy spectral density for different levels of tree branches for the lateral (a) and normal (b) motion described by (8) and (20), respectively. Red: outer branch; green: top branch, blue: middle branch; black: stem.

2.4. Laboratory experiments

The theory presented above is quite detailed insofar as its accounting of the kinetic and potential energy associated with each tree branch, however, for reasons of analytical tractability, it does not consider complexities of ambient flow such as vortex shedding and the spatial and temporal non-uniformity of the wind, *etc.* In order to assess whether the above theoretical predictions are representative, a series of experiments were conducted using a model tree-like structure that was constructed from 1.55 mm thick sheets of aluminum alloy 6061. As illustrated in Figure 5, the stem, which consisted of two aluminum sheets affixed together, measured 10.2 cm wide and was screwed to the base of the 8.9 cm tall wooden base which maintained the tree-like structure in an upright position. The stem extended unhindered 15.2 cm above the base. At its top, two branches each consisting of a single aluminum sheet were attached. The branches measured 5.1 cm $\times$ 17.8 cm and were positioned at an angle of 45° relative to the horizontal. This was

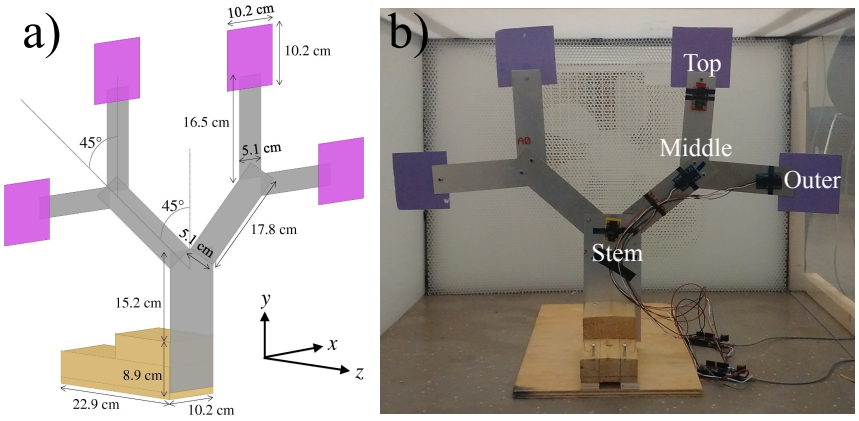

Figure 5: The model tree-like structure used in laboratory experiments. (a) A sketch of the tree-like structure in the erect orientation. The stem consisted of two sheets of aluminum affixed together whereas all the other branches were made from a single aluminum sheet. The entire tree-like structure measured 56.5 cm tall × 71.1 cm wide. (b) A photograph of the tree-like structure inside a small, open-loop wind tunnel, showing the attachment of accelerometers which are located on the downwind side of the tree. The box fan is just visible behind the honeycomb sheets. Accelerometers are attached to the branches and stem on the right-hand side of the tree.

followed by a second bifurcation such that two 5.1 cm × 16.5 cm branches were fastened to the tip of each primary branch. The secondary branches also consisted of single sheets of aluminum and were also attached at angles of 45°. Thus, the outer and top branches were respectively oriented in the horizontal and vertical directions. Note also that near the tip of each secondary branch was placed a 10.2 cm × 10.2 cm 'leaf' made from cardboard. Because of the scale of these leaves, a substantially larger amount of forcing was applied to the tips of the top and outer branches as compared to the rest of these branches. Q12

For purposes of collecting quantitative data, four OSSEP accelerometers each having 13 bit resolution were attached to different branches of the tree-like structure as in Figure 5, b). Accelerometers were individually connected to one of two OSEPP UNO R3 Plus boards so that acceleration information from any two accelerometers could be recorded simultaneously. Data was collected every 10 ms, the shortest time interval allowed by the experimental hardware. With reference to Figure 3, the accelerometers were oriented so that an erect tree-like structure corresponded to the z axis of each accelerometer being parallel to the ground. The accelerometers were capable of measuring accelerations in three coordinate directions. However, the most interesting mo- Q13 Q13

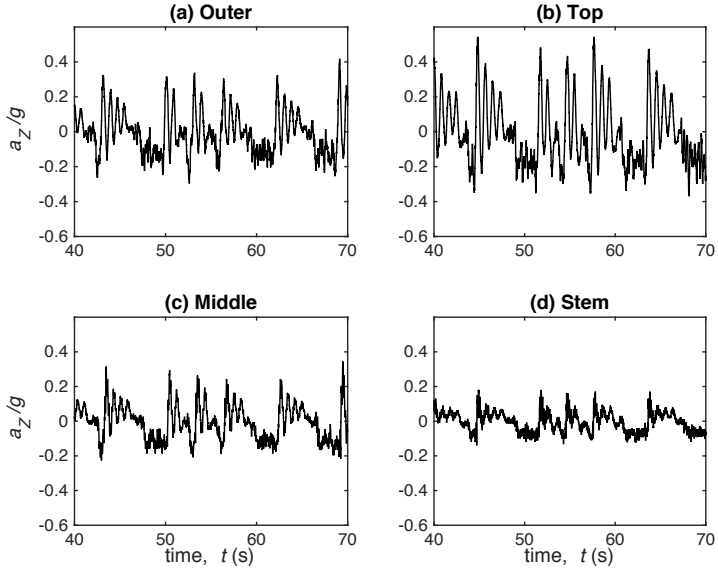

Figure 6: Acceleration measurements in the surface normal direction, Z. Naming of the accelerometers in panels (a-d) follows the convention of Figure 5 b.

tion, both in amplitude and in terms of features observed, was in the Z direction normal to the flat surface of both the accelerometer and the branches. (We label the associated acceleration a_Z.) Accordingly, acceleration measurements included some component of gravitational acceleration except, of course, when the tree-like structure was oriented in the erect position shown schematically in Figure 5 for which z and Z were antiparallel.

In general, most professional wind tunnels, particularly large closed-loop tunnels cannot provide quick ($\lesssim 1$ s) changes in the wind speed due to the large mass of moving air. The fastest shutoff and subsequent wind speed ramp-up using automatic control mechanisms is usually tens of seconds, which is substantially larger than all time scales relevant for the motion of the tree-like structure [33]. Thus, we constructed a smaller scale, open-loop wind tunnel, tailored for this experiment. The interior dimensions of our tunnel were 61 cm tall $\times$ 86 cm wide and the wind tunnel length was approximately 1.8 m, with smooth walls to prevent any internal vortex shedding inside the tunnel. These sizes were chosen so the tree-like structure occupied most of the available inner space without being unduly influenced by boundary effects. Air flow was produced using a three-speed 53 cm $\times$ 53 cm box fan, which was set to its highest speed. Just downstream of the fan was a 55 cm

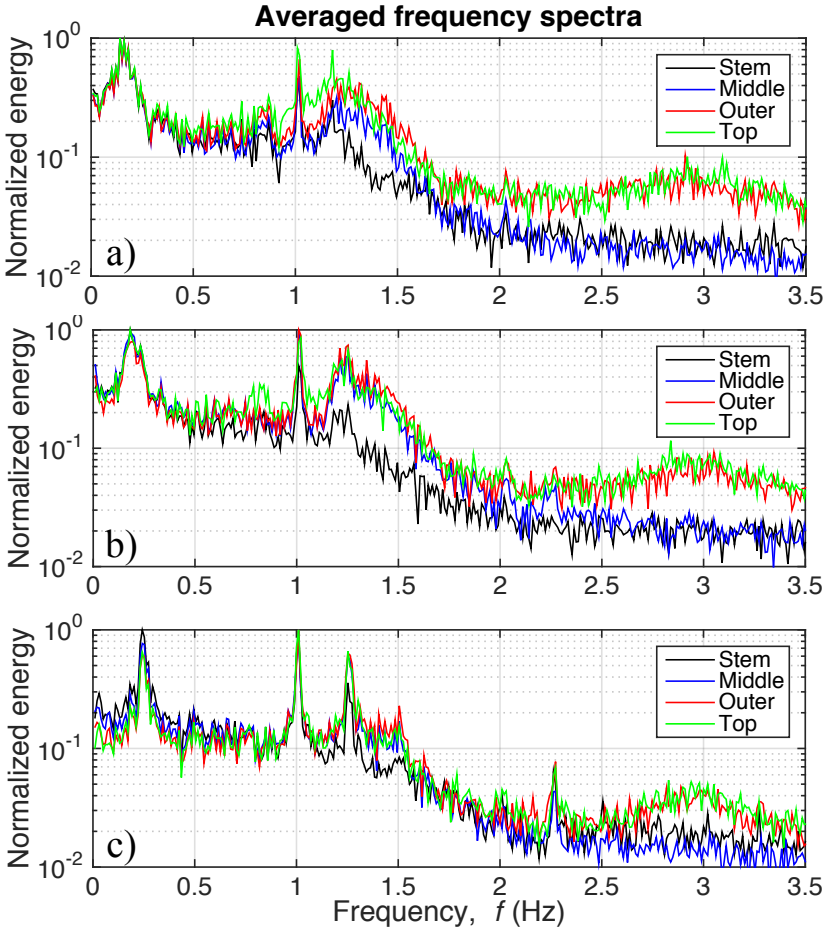

Figure 7: Normalized averaged frequency spectra for Levels 0, 1 and 2 as measured using the tree-like structure shown in Figure 5. Each curve corresponds to the average spectrum of nine independent experimental trials. Panel a): forcing intervals between 1 s and 4 s, Panel b): forcing intervals between 1 s and 3 s, Panel c): forcing intervals are either 1 s or 2 s. Signal regularization of the stem is most apparent in the Panel b).

long expansion zone and downstream of this were located two honeycomb sheets for flow laminarization that spanned the cross-sectional area of the wind tunnel. Each honeycomb sheet was 2.54 cm long and contained circular cells 8 mm in diameter. The tree-like structure was located approximately 57 cm downstream of the latter honeycomb sheet. At this position, we measured an air speed of $5.3\,\mathrm{km/h} \pm 0.2\,\mathrm{km/h}$ using a Super Scientific vane probe anemometer where the vane axis was located at an elevation of 32 cm from the bottom boundary. Wind speed measurements were made with the tree-like structure outside of the wind tunnel. The air flow quality was estimated by observing the tree-like structure at the maximum wind speed, where very little fluctuations of the structure were observed.

Immediately upstream of the box fan was a large sheet, which could be set to either a 'closed' or 'open' configuration. In the former, the sheet completely covered the upstream surface of the fan resulting in negligible air flow down the length of the wind tunnel. Measurements of the wind speed using a vane probe confirmed effectively complete blockage of the flow. Additionally, in the 'closed' configuration, no deformation of the tree-like structure was observed from its equilibrium position, defined as the erect position with the fan turned off. Q14 In the 'open' configuration, by contrast, the wooden sheet was lifted away from the fan and thus did not impede the motion of the incoming air. Using this set-up, a switch from the 'open' to 'closed' configuration took a fraction of a second, resulting in a similarly sharp change from zero to maximum air speed inside the tunnel.

Experiments were grouped according to the distribution of forcing time intervals when the system was in either the closed or open configuration. In the first group of experiments, the intervals consisted of a random sequence of 1 s and 2 s time intervals. For the second (resp., third) groups of experiments, we chose time intervals of 1 s, 2 s and 3 s (resp., 1 s, 2 s, 3 s and 4 s), each interval occurring with the probability of 1/3 (resp., 1/4). The length of these intervals was chosen intentionally, as it takes approximately a second or less for the flow to become established, and the motion of the tree-like structure substantially decreases after 4 s.

Each of the three groups of experiments consisted of nine independent trials. In total, therefore, we ran 54 experiments, each of which lasted 100 s. Since the typical oscillation time for each level was $\sim 0.1\,\mathrm{s}$ - 1 s, there were approximately $5 \cdot 10^3 - 10^4$ oscillations recorded with a typical resolution of 10 ms, or $10 - 100$ data points per one cycle of oscillation. This number of experimental runs and the commensurate volume of measured data was

deemed to be sufficient to provide accurate statistics for the computations of spectra of each level. Further to this point, and for each experimental trial, we ran two 100 s-long experiments in order to collect a full data set comprising acceleration information from Levels 0, 1 and 2.

Sample laboratory results from a particular experimental trial and spanning a 30 s time interval are shown in Figure 6. Motions between different levels are mostly synchronized *e.g.* there is a sharp increase of acceleration that is experienced at Levels 0, 1 and 2 at approximately 45 s. It is also apparent, however, that the timeseries signal for Level 0 (Figure 6 d) is less noisy than those for Level 2 (Figures 6 a,b). This suggests that the motion of the stem is characterized by lesser high-frequency components, a hypothesis that is confirmed by Figure 7. For each of the stem and the diagonal (middle), outer and top branches, Figure 7 shows the associated frequency spectra, derived from the average of the nine experimental trials that comprise each group of experiments. Our data confirm the regularization of the motion produced by the tree-like structure. Comparing Figures 4 and 7 indicates that the regularization in both the model calculations and the measured data is manifested by a reduction of the harmonic content of the stem compared to the spectra of the other branches.

2.5. Asymmetric trees and parameter studies

Until now, all our studies have focused on tree-like structures that were symmetric with respect to reflections about the vertical axis in the equilibrium state. In order to broaden our scope and investigate the robustness of the band-narrowing phenomenon for different tree configurations, we have also studied the response of geometrically asymmetric trees to the on-off forcing considered above. There are many ways in which asymmetries can be introduced. For brevity, we limit ourselves to the case where the ratios $L_1/L_0 = 0.5 \ldots 1.5$ and $L_{11}/L_0 = L_{21}/L_0 = 0.5 \ldots 1.5$ are varied with $L_{12} = L_{22} = L_0$. All other material properties and forcing details are as described in Sec. 2.1. Asymmetries could also be introduced by selectively changing branch angles away from $45°$, but we shall defer a detailed investigation of this possibility to a future study. We observe that the details of the resulting spectra for each branch do vary with the change of parameters. The results of our studies are summarized in Figure 8. A total of 20 simulations per ratio, *i.e.*, 400 simulations total were performed. We found that it is not especially informative to present all the resulting spectra in a single figure, so we choose to represent the spectrum for each branch as a single number. While this Q11

is certainly a simplification, the above method allows one to visualize the results of all numerical studies in a concise and apparent manner.

We define the spectral parameter as follows. For a normalized spectrum with the main peak laying in the low frequencies like we have for the systems considered here, let us take the cumulative sum of the normalized spectrum $S_\bullet(f_i)$ defined as

$$\mathrm{C.S}_{\bullet,i} = \sum_{k=1}^{i} S_\bullet(f_i)\,. \tag{23}$$

The cumulative spectra for all branches tend to a constant value, denoted here as $\mathrm{C.S}_\bullet^\infty$, for large frequencies[1]. For a more narrow peaked spectrum, there are fewer higher harmonics, so the limiting value $\mathrm{C.S}_\bullet^\infty$ is lower. On the contrary, for a broader spectrum, the limiting value $\mathrm{C.S}_\bullet^\infty$ is higher. This is, of course, not an exact measurement of the spectrum breadth as one can identify examples that violate this rule. However, for the spectra we have obtained in this problem, the limiting value of the cumulative spectra does seem to provide some helpful information concerning regularity.

Figure 8 a presents the cumulative spectra corresponding to the normal motion of the tree-like structure shown in Figure 4 b. Conversely, Figure 8 b presents an example of the cumulative spectra for the experiments (left) corresponding to the middle panel of Figure 7. We draw the associated curves over different frequency ranges for experiment vs. theory because much more detailed information is available from the numerical simulations. In both panels, however, it is evident that the curves reach a spectral plateau. Finally, panels (c) and (d) of Figure 8 show the results of dynamics regularization, defined as the ratio of the limiting values of the corresponding cumulative sums $\mathrm{C.S}_0^\infty/\mathrm{C.S}_1^\infty$ for (c) and $\mathrm{C.S}_0^\infty/\mathrm{C.S}_{11}^\infty$ for (d). The results are obtained and visualized for the 400 simulations for different ratios of the branches as a single color plot. High levels on this plot correspond to a high degree of dynamical regularization. While this simplified spectral representation does have its limitations, we believe it is useful to represent such a study of the system dependence on parameters in a concise form. Q15

[1]Note that in (23), f_i denotes the frequency, elsewhere, $f_\bullet$ denotes forcing. We hope the distinction is clear from the context.

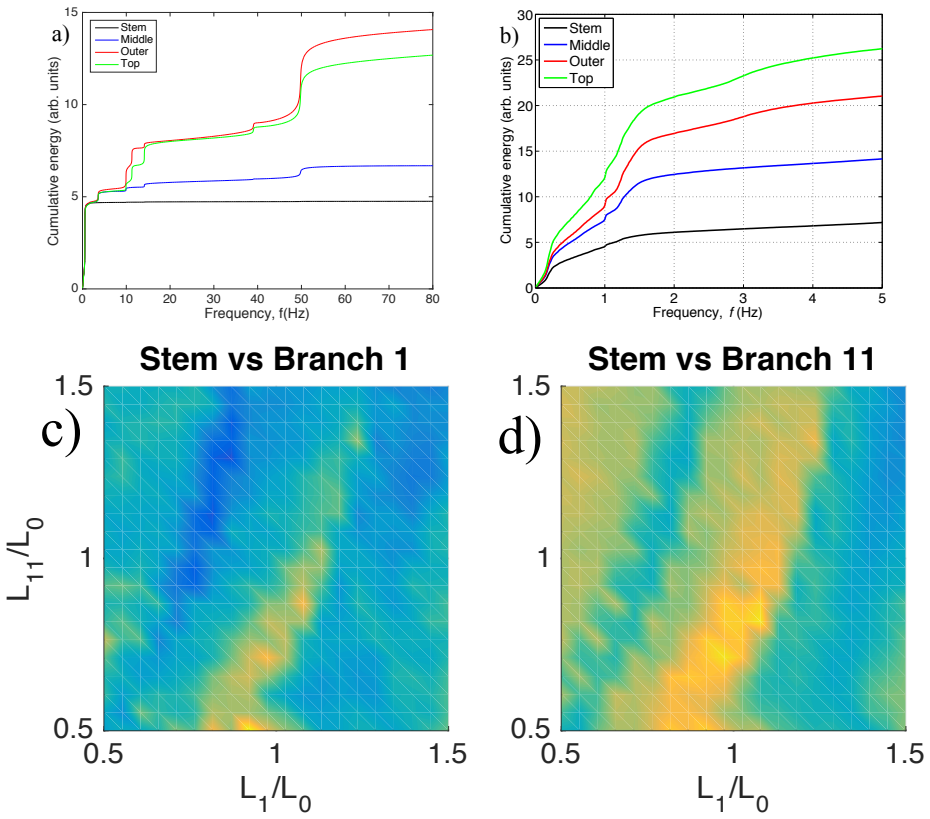

Figure 8: Panel (a): Cumulative spectra $C.S_0$, $C.S_1$, $C.S_{11}$ and $C.S_{12}$ for the normal oscillation described by equation (20). Panel (b): analogous results for the data presented in Figure 7 b. Panels (c) and (d): ratios of the limiting values of cumulative spectra $C.S_0^\infty/C.S_1^\infty$ for (c) and $C.S_0^\infty/C.S_{11}^\infty$ for (d) as defined by (23). In panels (c) and (d), high levels are yellow and low levels are blue.

3. On the nonlinear dynamical response of the tree-like structure

In order to further connect our work with the previous literature, it is also of interest to compute the fully nonlinear response of the system to a monochromatic (harmonic) forcing. While harmonic forcing is certainly quite different than the large bandwidth forcing studied in the previous section, in our opinion, it also gives an interesting insight into the fully nonlinear dynamics of the problem. There has been substantial interest in strongly nonlinear dynamics of a single resonator, one of the key effects being the presence of nonlinear resonances in an elastic beam [34]. Given a forcing

$f \sim \cos \omega t$, the nonlinear resonance leads to a broadening of the amplitude response $A(\omega)$. As a result, high frequencies are channelled to lower ones.

Following this methodology, we investigate the response of a 3D bending of a tree-like structure to a harmonic forcing applied to the top branches, *i.e.*, we simulate equations (20) with forcing $f_\bullet = A_\bullet \cos \omega t$. For this particular simulation, we suppose that the harmonic forcing only acts on the top branches. In our opinion, this allows us to drastically reduce the number of parameters and to streamline the presentation. The forcing amplitude, $A_\bullet$, is taken to be sufficiently large to ensure that the system is in a fully nonlinear regime. The physical parameters are identical to those used in Sec. 2.2. The results of our simulations are shown in Figure 9. All branches have nonlinear resonances at approximately the same values of ω. However, the nonlinear response of the stem is mostly in the low frequencies, whereas the other branches respond in both the low and high frequency regimes. The small 'bumps' in the amplitude response at ~ 25 and ~ 125 Hz correspond to the secondary resonances of the interconnected system, which are unavoidably smaller than the response at the main resonance frequencies. This nonlinear behavior may additionally explain the band narrowing we have discussed in this paper. Q17

It is also worth noting the relationship between the linear and nonlinear dynamics of the tree-like structures. In the purely linear framework, subsequent tree branches act as low-pass filters. The response of the stem to a particular force can then be computed as an appropriate sequential application of linear filters. Evidence for the incompleteness of this explanation comes from Appendix B, where we discuss the simulation of a planar analogue of a tree-like structure based on nonlinear springs. The simulation results in Figure B.11 confirm that there is a discrepancy of several orders of magnitude between the linear and nonlinear regimes for higher frequencies. This discrepancy is essential for understanding the presence of a more regular signal at the stem when truly broadband forcing is considered. This opens up an interesting question as to the relevance of the synchronization of adjacent branches as coupled nonlinear resonators [1] for the tree-like topology. While there is a large amount of work on the synchronization of resonators coupled in a line topology [35], synchronization in nontrivial tree-like topologies as studied here has not been studied to our best knowledge and therefore represents an interesting topic to consider in future.

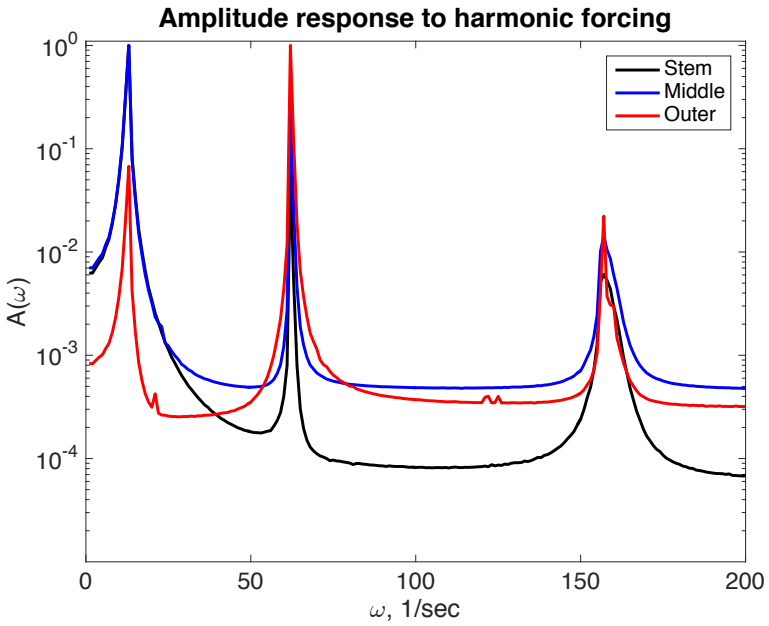

Figure 9: Amplitude response of the tree structure to a monochromatic forcing, for the stem (black line), middle level branch 1 (blue line), and top branch 11 (red line).

4. Conclusions and remarks on further studies

We have outlined a method of regularizing a broadband signal using tree-like structures. This method of exploiting the topology of the resonator in addition to nonlinearity is quite different from the methods presented in the literature, and may lead to the design and development of more efficient energy-harvesting devices. Moreover, the regularization of oscillatory motion observed in both theory and experiments opens the way to generating power directly in AC form using electromagnetic induction. For example, and for a macro-scale device, one can generate power by coupling the stem to a flywheel and a generator. In such devices, phase regulation is important to avoid an undesirable electromagnetic reaction. The mechanical impedances related to AC power production should also be carefully treated. Such interesting mechanical problems will, of course, go far beyond the simplistic models for friction used herein and will necessitate a coupling of the tree-like structure to the flywheel. We intend to study these topics in future, paying particular attention to the question of system optimization. On the one hand, the flywheel and generator should be powerful enough to operate with maximum efficiency. On the other hand, the effect on the stem should be small enough so as not to destroy its regular oscillation. Electric power conversion from a small-scale AC generator to any commercial AC power is key to power electronics [36]. One of the ways to model such energy conversion is to add appropriate inertia-like terms in the mechanical models. Topics like impedance matching or efficient active rectifiers [37] also play a crucial role in the development of such systems and their linkage to external power sources. Here again, and motivated by the present analysis, we plan to investigate these topics in forthcoming studies.

Another interesting direction, crucial for miniaturization, would be to use elements exhibiting highly nonlinear elasticity due to their geometric form, such as elastic spheres forming the basis of Hertz chains [38] or other geometric structures exhibiting a highly nonlinear response to compression. An alternative to using such elements would be to use excessively soft and highly nonlinear materials, although it is unclear that materials having the full range of requisite elastic properties are currently available. In any case, more research into the miniaturization of these devices seems warranted as being potentially able to provide inexpensive, robust harvesting solutions for a variety of applications. Note finally that Duffing oscillators have been studied in the context of topology optimization in contexts both more general Q21

and specific than what we have described above. See in particular [39, 40] for an example of parameter and geometry optimization in the MEMS context.

Acknowledgments

Major funding for this project was generously provided by NSERC through the Discovery Grant (MRF and VP) and USRA (RN) programs. Additional funding was also provided by the University of Alberta (MKu, MKi). TH and MKu acknowledge support from JSPS KAKENHI (Grant-in-Aid Challenging Exploratory Research) #26630176 , and MKi #25820164. MKu also acknowledges support for foundations for improvement of prominent graduate school. The technical assistance of Mr. Bernie Faulkner and Mr. Rick Conrad from the University of Alberta Department of Mechanical Engineering is also gratefully acknowledged.

Appendix A. Bifurcation analysis of equilibria in two and three dimensions

Physically, one expects that when the tree has sufficient mass and the stem and branches have sufficient flexibility, the erect (or trivial) equilibrium position loses its stability and another shape is adopted. In order to quantify this result, we investigate the stability of this trivial equilibrium ($\varphi_0 = 0$, $\theta_0 = 0$) in systems (8) and (20) by varying the length coefficient k defined as

$$\ell_i = k\ell_{i,\mathrm{org}}, \quad \ell_{ij} = k\ell_{ij,\mathrm{org}}, \tag{A.1}$$

between 0.5 and 1.5. Assuming a uniform material density, the mass of each beam is proportional to its length so that $m_i = km_{i,\mathrm{org}}$, $m_{ij} = km_{ij\mathrm{org}}$. Specific length-scales for the elements of Figures 2 and 3 are presented in table A.1. Following experiments, we assume that the material of construction is aluminum, with a density $\rho_{\mathrm{Al}} = 2.70 \times 10^3\,\mathrm{kg/m^3}$ and a Young's modulus of $E_{\mathrm{Al}} = 7.0 \times 10^{10}\,\mathrm{Pa}$.

The natural frequency of each beam, if it were attached as a single cantilever, is given by Euler-Bernoulli beam theory as

$$f_\bullet = \frac{1}{2\pi}\frac{\lambda_1}{\ell_\bullet}\sqrt{\frac{E_{\mathrm{Al}}h_\bullet^2}{12\rho_{\mathrm{Al}}}}, \tag{A.2}$$

where $\lambda_1 = 1.87510\ldots$ is a constant for the frequency of the first-mode oscillation. In this Appendix, $f_\bullet$ denotes the frequency of the branch $\bullet$,

Table A.1: Branch size for each of the elements of Figures 2 and 3.

	Length		Width		Thickness		Mass	
Layer 0 (0)	ℓ_0	45.7 cm	w_0	5.08 cm	h_0	0.813 mm	m_0	$\rho_{\mathrm{Al}}\ell_0 w_0 h_0$
Layer 1 (i)	ℓ_i	$k{\cdot}17.8$ cm	w_i	w_0	h_i	h_0	m_i	$\rho_{\mathrm{Al}}\ell_i w_i h_i$
Layer 2 (ij)	ℓ_{ij}	$k{\cdot}16.5$ cm	w_{ij}	w_0	h_{ij}	h_0	m_{ij}	$\rho_{\mathrm{Al}}\ell_{ij} w_{ij} h_{ij}$
Top/side weight	$\ell_{\mathrm{w}ij}$	10.2 cm	w_{ij}^{W}	10.2 cm	h_{ij}^{W}	0.813 mm	m_{ij}^{W}	$\rho_{\mathrm{Al}}\ell_{ij}^{\mathrm{W}} w_{ij}^{\mathrm{W}} h_{ij}^{\mathrm{W}}$

Table A.2: Coefficient values corresponding to (5-10) and (20).

	α	β	γ	A
Layer 0 (0)	$(2\pi f_0)^2 m_0 \ell_0^2/3$	$\alpha_0/10$	$\Gamma\ell_0 w_0$	$C\ell_0 w_0$
Layer 1 (i)	$(2\pi f_i)^2 m_i \ell_i^2/3$	$\alpha_i/10$	$\Gamma\ell_i w_i$	$C\ell_i w_i$
Layer 2 (ij)	$(2\pi f_{ij})^2 m_{ij} \ell_{ij}^2/3$	$\alpha_{ij}/10$	$\Gamma(\ell_{ij} w_{ij} + \ell_{ij}^{\mathrm{W}} w_{ij}^{\mathrm{W}})$	$C(\ell_{ij} w_{ij} + 2\ell_{ij}^{\mathrm{W}} w_{ij}^{\mathrm{W}})$

not the force acting on it. The linear coefficients in (6) are determined from the size and natural frequency of the branches, whereas the nonlinear coefficients are assumed, for simplicity, to be one-tenth the magnitude of the corresponding linear coefficients. Table A.2 summarizes the parameters used in the simulations. We set gravitational acceleration to be $g = 9.8\,\mathrm{m/s^2}$ and the damping coefficient per unit area to be $\Gamma = 0.1\,\mathrm{N{\cdot}m\,s/m^2}$. The amplitude of forcing applied to the tree per unit area is set by the coefficient $C = 1\,\mathrm{N{\cdot}m/m^2}$.

Figure A.10 shows the associated bifurcation diagrams for the two-dimensional planar and normal oscillatory motions. For small values of the length coefficient k, the trivial equilibrium is stable. As k approaches 1.1 , however, the equilibrium loses its stability and two stable "leaning" equilibria appear in the system. Thus, depending on the parameters, the flexible tree-like structure can be used in both the stable (small k) and bi-stable regimes, with the latter being particularly useful for broadband energy harvesting applications [13].

Appendix B. Planar structures and energy harvesting

Appendix B.1. Dynamics and band narrowing in planar tree-like structures

In this section, we consider alternative designs utilizing the tree-like topology where the motion is confined to a single dimension. This section is motivated by the recent work on the parallel arrangement of multiple resonators

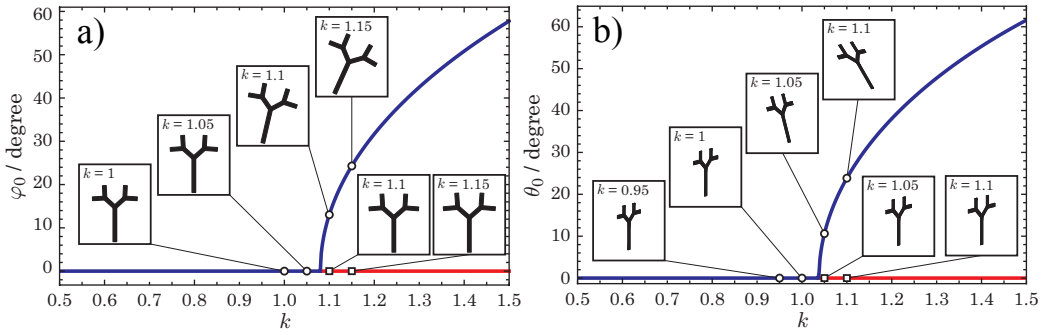

Figure A.10: Bifurcation diagram with respect to k, defined by (A.1). (a) Lateral (in-plane) deformation. (b) Normal (out-of-plane) deformation.

and the corresponding broadening of the response function for a composite harvesting device [41, 42, 43, 44]. Such mechanical devices are gaining popularity as they can be applied at smaller scales, enclosed in relatively compact and sealed containers and may thus be beneficial for industrial deployment. Here we outline the design of a device with a tree-like topology and summarize the corresponding increase in efficiency compared with the arrangement of parallel nonlinear oscillators.

Figure B.11 a exhibits a model planar energy harvester where each mass on the n^{th} level is connected via nonlinear springs to a given number of masses on the next level, $n + 1$. Our schematic shows only three levels with two masses each, however more levels and different configurations are, of course, possible. The equations of motion for this system are easily derived using the previous Lagrangian method. Let $x_\bullet$ represent the displacement with respect to a fixed frame of a particular spring from its equilibrium position. Consistent with the previous discussion, $\bullet$ may denote any of "$_0$", "$_i$" or "$_{ij}$". In what follows, we shall assume that the time scale has been chosen to correspond to the typical time scale of the system, and shall therefore make reference to the appropriately normalized non-dimensional variables. Corresponding planar velocities are denoted by $\dot{x}_\bullet$. If $U_\bullet(x)$ is the (non-dimensional) potential energy of each spring, and $V_j(x)$ accounts for the

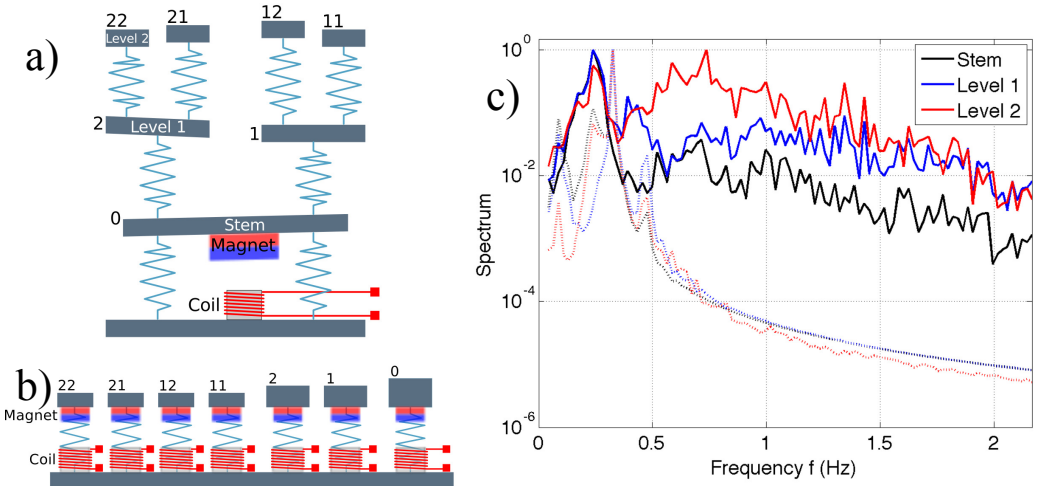

Figure B.11: (a) Schematic of a planar design for energy harvesting mimicking the tree geometry. (b) Assembly of seven parallel oscillators with exactly the same properties as the oscillators from the top panel. (c) Numerically-determined spectra for the 2D energy harvester exhibited in (a). Data correspond to the average of ten simulations. Dotted lines of the same colour show the results for the linear system subject to exactly the same forcing as the nonlinear system. While overall regularity of motion is higher for the linear system, there is no pronounced band-narrowing towards the stem in the linear case.

coupling between springs, the Lagrangian reads

$$\mathcal{L}(\mathbf{x},\dot{\mathbf{x}}) = \frac{1}{2}\sum_{\bullet}\dot{x}_{\bullet}^2 - \frac{1}{2}\left[U_0(x_0) + U_1(x_0-x_1) + U_2(x_0-x_2)\right.$$
$$+ U_{11}(x_1-x_{11}) + U_{12}(x_1-x_{12}) + U_{21}(x_2-x_{21}) + U_{22}(x_2-x_{22}) \quad \text{(B.1)}$$
$$\left. + \left(V_1(x_1-x_2) + V_2(x_{11}-x_{12}) + V_2(x_{21}-x_{22})\right)\right] .$$

The equations of motion are written in their non-dimensional form as

$$\ddot{x}_{\bullet} - \frac{\partial \mathcal{L}}{\partial x_{\bullet}} + \nu_{\bullet}\dot{x}_{\bullet} + F_{\bullet}(t) = 0, \quad \text{(B.2)}$$

with $F_{\bullet}$ being the non-dimensional external force acting on the branch $\bullet$. In this notation, we use nonlinear springs having a Duffing-like potential energy given by $U_{\bullet} = \omega_{\bullet}^2(x^2/2 + \beta x^4/4)$. The linear coupling between oscillators is given by $V(x) = \lambda x^2/2$. In what follows, we shall assume that all natural linear frequencies are identical, *i.e.*, $\omega_{\bullet} = \omega$ and choose the normalization of

the time scale so that $\omega = 1$. Equations (B.2) are derived from the Euler-Lagrange equations, with additional dissipation terms that may represent either mechanical friction or energy withdrawal due to harvesting. A justification for this approach is provided below. For simplicity, gravity terms are omitted, which is a reasonable approximation for small-scale devices. The introduction of gravity terms, relevant for larger scale devices, does not change the band-narrowing behaviour, as long as the structure remains stable to gravitational forces.

Figure B.11 c shows the results of a numerical simulation of (B.2) with non-dimensional values $\beta = 1$, $\lambda = 1$ and $\nu = 0.01$, in order to demonstrate the effect of relatively large nonlinearity and coupling compared to friction forces. The force $F_i(t)$, which is applied to the top four oscillators, jumps between zero and a constant value at the pre-determined points $t = t_k$ with $t_{k+1} - t_k$ chosen at random before the start of each run. Figure B.11 c considers the average frequency spectra as computed from ten individual numerical simulations. As in Figures 4 and 7, the averaged results are normalized so that the maximum for each spectrum is exactly unity. The spectrum is regularized in going from Level 2 to Level 1 to the stem, Level 0. Note, in particular, that while the peak remains the same, the harmonics higher than about 0.3 apparently diminish in relative significance. For comparison, the same panel includes simulations of a design of the same topology but consisting of linear strings, *i.e.* imposing $\beta = 0$ with all other parameters and forcing being unchanged from the nonlinear case. The results of the linear system evolution, represented with the dotted curves, show no significant signal regularization towards the stem, as the tails of the spectrum almost overlap. This is in agreement with the concept of band-narrowing outlined on Figure 1. Q20
When the high frequency modes get re-arranged by a nonlinear response, they inevitably have noisier structure in the high frequencies. By contrast, the linear oscillator acts as a linear filter, so the high frequency part of the spectrum is almost identical for different levels and much smoother compared to the nonlinear counterpart. Thus, we believe that the observed signal regularization cannot be described by a purely linear theory. One should note that the tails of the spectrum for the linear case are substantially below those of the nonlinear case, so the response of the linear system to a broadband force is inherently more regular as compared to the nonlinear system. However, this regularization for the linear system is uniform for all branches, since a linear filter would Q3
simply multiply the spectrum by an appropriate filter function. As we have noted in the Introduction and illustrated in Figure 1, the persistence of high-frequency

harmonics is indicative of signal regularization rather than application of a linear filter.

Appendix B.2. Energy harvesting efficacy of the tree-like design vs. parallel oscillator arrangement

We now make a comparison between the energy-harvesting efficiency of the branched and parallel designs shown, respectively, in the panels a) and b) of Figure B.11. This will allow us to clarify the advantages and disadvantages of our design, as compared with the classical nonlinear oscillator designs established in the literature. While power harvesting is not the focus of this paper, we found this comparison to be interesting and useful to make.

The potential energy for each oscillator is given by $U_\bullet(x) = \omega_\bullet^2(x^2/2 + \beta x^4/4)$; for this particular simulation we have taken the spring nonlinearity $\beta = 0.007$ corresponding to the typical measured nonlinearity of available small-scale springs for the planar design shown in Figure B.11 a. For simplicity, all variables in this section are dimensionless, with the period being non-dimensionalized by the smallest resonance frequency of the individual oscillator, and the displacement, x, non-dimensionalized by a typical static displacement value computed from the static force. The energy coupling term is given by $V_\bullet(x) = \lambda x^2/2$ where the coupling coefficient, λ, has a value of 0.01. The natural linear frequencies are chosen to be $\omega_0 = 2\pi$, $\omega_i = 4\pi$ and $\omega_{ij} = 6\pi$ for $i, j = 1, 2$. The dissipation term $(\nu_0 + \nu_h)\dot{x}_\bullet$ consists of two contributions, namely, a mechanical dissipation term proportional to ν_0 and an energy harvesting term proportional to ν_h. This dissipation term for energy harvesting can be justified for an induction-based generator, as the voltage W caused by induction is proportional to the velocity, *i.e.*, $W_\bullet = K_\bullet \dot{x}_\bullet$, see *e.g.*, [45, 46]. Here, we have introduced the induction coefficient $K_\bullet$ which depends on the oscillator. For the simplest possible load, a resistance R, the power, $PC_\bullet$, consumed at branch $\bullet$ is

$$PC_\bullet = \frac{W_\bullet^2}{R} = \frac{1}{R} K_\bullet^2 \dot{x}_\bullet^2 := \nu_{h,\bullet} \dot{x}_\bullet^2 \,.$$

The model of harvesting used here, while certainly simplistic, has the advantage of employing only a few parameters which are essential for drawing a proper comparison between a tree-like and parallel oscillator. We enforce the normalization for the comparison as follows. First, we set the net force applied to the two systems to be identical. Second, we set the dissipation $\nu_\bullet = \nu = 0.01$ for all oscillators in the parallel and tree-like design, which is

equivalent to the assumption that all resonators have a similar design and are constructed from similar material. Third, in the case of the parallel assembly, each of the seven oscillators is assigned the harvesting coefficient $\nu_{h,\bullet} = \nu_h = 0.03$. For the tree-like assembly, we select $\nu_{h,0} = 0.21$ at the stem, the location where the harvesting is applied, with $\nu_{h,i} = \nu_{h,ij} = 0$ elsewhere. The total harvesting potential for the branched assembly is therefore equal to the parallel assembly, and any discrepancy in harvesting outcomes must be due to the efficacy of the harvester itself.

In principle, if the load is more complex than a simple resistor, consisting, for example, of an LRC circuit, computation of harvesting efficacy is more complicated and will need to include another ODE to be solved in conjunction with the original system. This complex harvesting mechanism will introduce additional parameters and therefore falls outside of the scope of the present inquiry.

In light of the above, the energy harvested by the system is computed via

$$E = \int_{t_0}^{T} \sum_{\bullet} \nu_h \dot{x}_{\bullet}^2 \,, \tag{B.3}$$

where the sampling interval boundaries $t_0 = 100$ and $T = 220$ are sufficiently large to remove all initial transient behaviours. Results from solving (B.2) using (B.3) are presented in Figure B.12. The efficacy of harvesting of the branched design, shown in Figure B.11 a, compared to its parallel counterpart, shown in panel (b), increases as the forcing becomes more and more broadband. When the forcing is fully broadband, the branched structure harvests more than 100 times as much energy as the parallel design. On the other hand, when the forcing contains less than approximately 30 distinct frequencies, the parallel assembly offers superior performance.

Appendix C. General theory of dynamics for tree-like structures in three dimensions

In this Appendix, we briefly touch upon the general theory of the dynamics for tree-like structures. This derivation follows the general mathematical theory outlined in [31] and an abstract mathematical approach describing the dynamics of nested semidirect products, conservation laws and Poisson brackets. For brevity, we shall only focus on two-level trees like the one presented in our paper. Trees with deeper structures can easily be considered, but the formulas become cumbersome to write down.

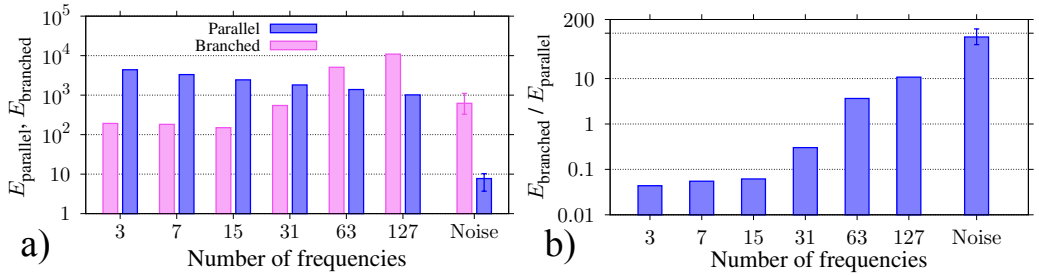

Figure B.12: Comparison of the energy produced by the branched design (E_{branched}) vs. the corresponding parallel assembly (E_{parallel}) illustrated in Figure B.11. (a) Energy harvested for each design in different cases as a function of the irregularity of forcing. (b) Ratio of the bar graph data from the left-hand side panel. In either case, the horizontal axis specifies the number of harmonics present in the applied forcing, with random forcing being shown as the rightmost column.

Consider a tree-like structure with branches 0, i, ij, corresponding, in our notation, to the stem, first and second levels. The orientation of a branch is given by the orientation matrix $\mathbf{A}_\bullet \in SO(3)$, with $\mathbf{A}_\bullet \mathbf{A}_\bullet^T = \mathrm{Id}_{3\times 3}$, where the orientation can be taken either with respect to a fixed frame or, alternatively, with respect to the orientation of the branch immediately preceding it on the tree structure. We use $\bullet$ to denote the index of the corresponding branch. If we choose a coordinate transformation with respect to the previous frame on the branch, then the center of mass of each beam is represented as

$$\mathbf{r}_0 = \mathbf{c}_0, \quad \mathbf{r}_i = \mathbf{c}_i + 2\mathbf{c}_0, \quad \mathbf{r}_{ij} = \mathbf{c}_{ij} + 2\mathbf{c}_i + 2\mathbf{c}_0, \quad \mathbf{r}_{ij}^{\mathrm{W}} = 2\mathbf{c}_{ij} + 2\mathbf{c}_i + 2\mathbf{c}_0, \tag{C.1}$$

where $\mathbf{c}_\bullet$ is defined as

$$\mathbf{c}_0 = \mathbf{A}_0^{-1}\mathbf{c}_0', \quad \mathbf{c}_i = (\mathbf{A}_0\mathbf{A}_i)^{-1}\mathbf{c}_i', \quad \mathbf{c}_{ij} = (\mathbf{A}_0\mathbf{A}_i\mathbf{A}_{ij})^{-1}\mathbf{c}_{ij}' \,. \tag{C.2}$$

Here $\mathbf{c}_\bullet' = (0, \ell_\bullet/2, 0)^T$ is a position vector of the center of mass in each local coordinate system, *i.e.*, the center of mass in the undisturbed position is along the y-axis. We have assumed that the stem orientation (index '0') is computed with respect to a fixed frame. Moreover, we have followed the definitions of Sec. 2.2, which gives the product of matrices in the order shown by (C.2). Alternative definitions are possible, for example, taking matrices of transformations to be the inverse of what is defined here, which will modify (C.2) accordingly. The kinetic energy of translational motion is then obtained

by taking time derivatives of the coordinates as

$$K_{\text{vel}} = \frac{1}{2}m_0|\dot{\mathbf{r}}_0|^2 + \sum_i \frac{1}{2}m_i|\dot{\mathbf{r}}_i|^2 + \sum_{i,j} \frac{1}{2}m_{ij}|\dot{\mathbf{r}}_{ij}|^2 + \sum_{i,j} \frac{1}{2}m_{ij}^{\text{W}} \left|\dot{\mathbf{r}}_{ij}^{\text{W}}\right|^2. \quad \text{(C.3)}$$

The change in coordinates occurs due to the corresponding change in the rotation matrices $\mathbf{A}_\bullet$, and to finalize the equations of motion, one needs to choose a parameterization of $\mathbf{A}_\bullet$ brought about by an appropriate choice of coordinates on the rotation matrix group $SO(3)$. There are many ways to parameterize this group, such as the Euler angles, Tait-Bryan angles and quaternions. As an example, we shall choose the Euler angles, defining a coordinate transformation as

$$\mathbf{x}' = \mathbf{A}(\theta, \varphi, \psi)\mathbf{x}, \quad \text{(C.4)}$$

where $\mathbf{A}(\theta, \varphi, \psi) = \mathbf{B}(\psi)\mathbf{C}(\theta)\mathbf{D}(\varphi)$ with the matrices $\mathbf{B}, \mathbf{C}$ and $\mathbf{D}$ defined as

$$\mathbf{B}(\psi) = \begin{pmatrix} \cos\psi & \sin\psi & 0 \\ -\sin\psi & \cos\psi & 0 \\ 0 & 0 & 1 \end{pmatrix}$$

$$\mathbf{C}(\theta) = \begin{pmatrix} 1 & 0 & 0 \\ 0 & \cos\theta & \sin\theta \\ 0 & -\sin\theta & \cos\theta \end{pmatrix}$$

$$\mathbf{D}(\varphi) = \begin{pmatrix} \cos\varphi & \sin\varphi & 0 \\ -\sin\varphi & \cos\varphi & 0 \\ 0 & 0 & 1 \end{pmatrix}.$$

Figure C.13 illustrates this coordinate transformation. For a particular realization of the coordinate transformation for modelling, we make a number of assumptions. Each beam is initially mounted with the angle φ, which is fixed in time, namely, $\varphi = \varphi^{\text{E}}$. The angle θ denotes the displacement angle of the beam, and rotation around z'-axis is prohibited because the bottom edge is fixed at the lower beam so $\psi = 0$. Therefore the matrix of the coordinate transformation becomes $\mathbf{A}_\bullet(\theta_\bullet, \varphi_\bullet^{\text{E}}, 0) = \mathbf{C}(\theta_\bullet)\mathbf{D}(\varphi_\bullet^{\text{E}})$.

If each coordinate system is allowed to rotate, we will need to compute the angular velocity of each beam as represented by the corresponding coordinate systems. In the local $\bullet$ coordinate system, the rotation of each beam is described by $\boldsymbol{\omega}'_\bullet = (\dot{\theta}_\bullet, 0, 0)^T$. Therefore, the resultant vector of rotation is obtained as follows:

$$\boldsymbol{\Omega}'_0 = \boldsymbol{\omega}_0, \quad \boldsymbol{\Omega}'_i = \boldsymbol{\omega}'_i + \mathbf{A}_i\boldsymbol{\Omega}'_0, \quad \boldsymbol{\Omega}'_{ij} = \boldsymbol{\omega}'_{ij} + \mathbf{A}_{ij}\boldsymbol{\Omega}'_i. \quad \text{(C.5)}$$

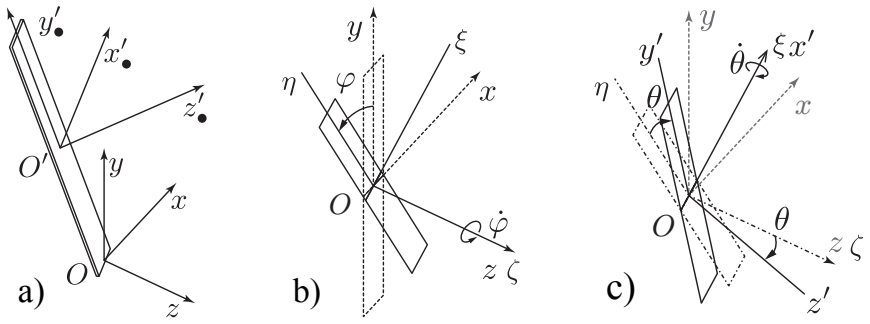

Figure C.13: Definition of angles of rotation and coordinate systems. (a) A view of the local coordinate system of branch $\bullet$, denoted $(x_\bullet, y_\bullet, z_\bullet)$, and the laboratory coordinate system denoted (x, y, z). (b) Rotated coordinate frame for consideration of two dimensional dynamics. (c) Definition of Euler angles for a rotated coordinate frame for 3D dynamics, with the coordinate frames (x', y', z') and (x, y, z) corresponding to the branch's coordinate frame and the coordinate frame of the previous level, respectively. The angle of rotation around the z'-axis, ψ, is always zero in experiments because the bottom end of each beam is fixed.

As shown in Figure C.13, each axis corresponds to the principal axis of inertia. Therefore, the kinetic energy of rotation is simply

$$K_{\text{rot}} = \frac{1}{2}\mathbf{I}_0\boldsymbol{\Omega}'_0 \cdot \boldsymbol{\Omega}'_0 + \sum_i \frac{1}{2}\mathbf{I}_i\boldsymbol{\Omega}'_i \cdot \boldsymbol{\Omega}'_i + \sum_{i,j} \frac{1}{2}\mathbf{I}_{ij}\boldsymbol{\Omega}'_{ij} \cdot \boldsymbol{\Omega}'_{ij}, \tag{C.6}$$

where $\mathbf{a} \cdot \mathbf{b}$ denotes the scalar product between the 3D vectors $\mathbf{a}$ and $\mathbf{b}$ and the inertia matrices are defined as

$$\mathbf{I}_\bullet = \text{diag}(I_{\bullet x}, I_{\bullet y}, I_{\bullet z})^T = \text{diag}\left(\frac{m_\bullet \ell_\bullet^2}{12}, \frac{m_\bullet w_\bullet^2}{12}, \frac{m_\bullet(\ell_\bullet^2 + w_\bullet^2)}{12}\right). \tag{C.7}$$

The primes measure the angular velocities in the frame attached to the local branch, which allows for the computation of the rotational kinetic energy.

The potential energy of deformation, P_b, is taken as the lowest (quartic) Taylor approximation satisfying symmetry properties whence

$$P_b = \frac{1}{2}\alpha_0\theta_0^2 + \frac{1}{4}\beta_0\theta_0^4 + \sum_i \left(\frac{1}{2}\alpha_i\theta_i^2 + \frac{1}{4}\beta_i\theta_i^4\right) + \sum_{i,j} \left(\frac{1}{2}\alpha_{ij}\theta_{ij}^2 + \frac{1}{4}\beta_{ij}\theta_{ij}^4\right). \tag{C.8}$$

$$\tag{C.9}$$

Meanwhile the gravity potential is given by

$$P_g = m_0 g r_{0,y} + \sum_i (m_i g r_{i,y}) + \sum_{i,j} (m_{ij} g r_{ij,y}) + \sum_{i,j} (m_{ij}^{\mathrm{W}} g r_{ij,y}^{\mathrm{W}}) \,, \tag{C.10}$$

Here $r_{\bullet,y}$ represents the vertical-component of the position vector $\mathbf{r}_\bullet$, and g is gravitational acceleration. In general, the elastic potential energy depends on the relative rotation matrix between the branches, causing interesting mathematical consequences for the dynamics, see [31] for details. Next, the external force caused by a wind can be introduced as a potential energy

$$\begin{aligned} P_e = A_0 F_{\mathrm{ext}}(t) r_{0,z} + \sum_i A_i F_{\mathrm{ext}}(t) r_{i,z} \\ + \sum_{i,j} A_{ij} F_{\mathrm{ext}}(t) r_{ij,z} + \sum_{i,j} A_{ij}^{\mathrm{W}} F_{\mathrm{ext}}(t) r_{ij,z}^{\mathrm{W}} \,, \end{aligned} \tag{C.11}$$

where $A_\bullet$ is a coefficient proportional to the area of beam, namely, $A_\bullet \propto \ell_\bullet w_\bullet$. Note that the potential energy representation of the external force (C.11) is used here for convenience; in principle, one can introduce the external force directly into the Euler-Lagrange equations, which is useful for non-conservative forces.

In the most general approach, energy dissipation can be computed using the Rayleigh dissipation function. The dissipation is assumed to be proportional to the component of the velocity of the beam that is parallel to the normal vector $\mathbf{n}_\bullet$. Let $\mathbf{v}_0' = \mathbf{A}_0 \dot{\mathbf{r}}_0$, $\mathbf{v}_i' = \mathbf{A}_i \mathbf{A}_0 \dot{\mathbf{r}}_i$, $\mathbf{v}_{ij}' = \mathbf{A}_{ij} \mathbf{A}_i \mathbf{A}_0 \dot{\mathbf{r}}_{ij}$, $\mathbf{v}'^{\mathrm{W}}_{ij} = \mathbf{A}_{ij} \mathbf{A}_i \mathbf{A}_0 \dot{\mathbf{r}}^{\mathrm{W}}_{ij}$ be velocities described by the local coordinate system which is fixed at each beam. The Rayleigh dissipation function can then be taken as

$$\begin{aligned} \mathcal{F} = \frac{1}{2} \boldsymbol{\gamma}_0 \mathbf{v}_0' \cdot \mathbf{v}'_0 + \frac{1}{2} \sum_i \boldsymbol{\gamma}_i \mathbf{v}_i' \cdot \mathbf{v}'_i \\ + \frac{1}{2} \sum_{i,j} \boldsymbol{\gamma}_{ij} \mathbf{v}_{ij}' \cdot \mathbf{v}_{ij}' + \frac{1}{2} \sum_{i,j} \boldsymbol{\gamma}_{ij}^{\mathrm{W}} \mathbf{v}_{ij}' \cdot \mathbf{v}'^{\mathrm{W}}_{ij} \,, \end{aligned} \tag{C.12}$$

where $\boldsymbol{\gamma}_\bullet = \mathrm{diag}(\gamma_{x,\bullet}, \gamma_{y,\bullet}, \gamma_{z,\bullet})$ is the dissipation coefficient vector (matrix). We use relative branch velocity for computing the dissipation as we assume that most of the friction is coming from the relative motion of the branches. One can also incorporate a similar dissipation function based on the absolute branch velocities $\dot{\mathbf{r}}_\bullet$, providing an appropriate generalization of (C.12). The

dissipation in the z-direction in the local coordinate frame should be more significant because of the shape of beam. Therefore, the dissipation coefficient vector can be approximated as $\boldsymbol{\gamma}_\bullet \simeq \mathrm{diag}(0, 0, \gamma_\bullet)$, leading to the expression (10) for the dissipation function. Finally, the Euler-Lagrange equations are written as

$$\frac{\mathrm{d}}{\mathrm{d}t}\frac{\partial \mathcal{L}}{\partial \dot{\theta}_\bullet} - \frac{\partial \mathcal{L}}{\partial \theta_\bullet} + \frac{\partial \mathcal{F}}{\partial \dot{\theta}_\bullet} = 0, \tag{C.13}$$

where $\mathcal{L} = K_{\mathrm{rot}} + K_{\mathrm{vel}} - P_{\mathrm{g}} - P_{\mathrm{b}} - P_{\mathrm{e}}$. This approach can be generalized further when a particular branch has more than one degree of freedom, *i.e.*, when $\psi_\bullet$ and/or $\varphi_\bullet$ depend on time. Of course, this situation will make the equations of motion (C.13) substantially more complicated to write down and analyze. We refer the reader to [31] for the full mathematical exposition of the dynamical theory in this general case.

[1] S. Strogatz, Sync: How Order Emerges From Chaos In the Universe, Nature, and Daily Life, Hyperion, 2004.

[2] J. Twiefel, H. Westermann, Survey on broadband techniques for vibration energy harvesting, Journal of Intelligent Material Systems and Structures 24 (2013) 1291–1302.

[3] S. Li, H. Lipson, Vertical-stalk flapping-leaf generator for wind energy harvesting, in: Proceedings of SMASIS2009-1276, Oxnard, CA, USA, 2009.

[4] S. Roundy, P. K. Wright, J. Rabaey, A study of low level vibrations as a power source for wireless sensor nodes, Computer Communications 26 (2003) 1131–1144.

[5] F. Lu, H. P. Lee, S. P. Lim, Modeling and analysis of micro piezoelectric power generators for micro-electromechanical-systems applications, Smart Materials and Structures (2004) 57–63.

[6] X. He, Z. Shang, Y. Cheng, Y. Zhu, A micromachined low-frequency piezoelectric harvester for vibration and wind energy scavenging, Journal of Micromechanics and Microengineering 23 (2013) 125009.

[7] S. Wei, H. Hu, S. He, Modeling and experimental investigation of an impact-driven piezoelectric energy harvester from human motion, Smart Materials and Structures 22 (2013) 105020.

[8] D. F. Berdy, P. Srisungsitthisunti, B. Jung, X. Xu, J. F. Rhoads, D. Peroulis, Low-frequency meandering piezoelectric vibration energy harvester, IEEE Trans Ultrasonics, Ferroelectrics and Frequency Control (2012) 846–858.

[9] J. Kymissis, C. Kendall, J. Paradiso, N. Gershenfeld, Parasitic power harvesting in shoes, Proceeding of the Second IEEE International Conference on Wearable Computing.

[10] G. Despesse, J. Chaillout, T. Jager, J. Loger, A. Vassilev, S. Basrour, B.Charlot, High damping electrostatic system for vibration energy scavenging, Proceedings of Joint SOC-EUSAI conference.

[11] R. McInnes, D. G. Gorman, M. P. Cartmell, Enhanced vibrational energy harvesting using nonlinear stochastic resonance, Journal of Sound and Vibration 318 (2008) 655–662.

[12] J. Moehlis, B. E. DeMartini, J. L. Rogers, K. L. Turner, Exploiting nonlinearity to provide broadband energy harvesting, in: Proceedings of the ASME 2009 Dynamic Systems and Control Conference, Hollywood, CA, 2009.

[13] B. P. Mann, B. A. Owens, Investigations of a nonlinear energy harvester with a bistable potential well, Journal of Sound and Vibration 329 (2010) 1215–1226.

[14] F. Cottone, H. Vocca, L. Gammaitoni, Nonlinear energy harvesting, Physical Review Letters 102 (2009) 080601.

[15] S. C. Stanton, C. C. McGehee, B. P. Mann, Nonlinear dynamics for broadband energy harvesting: Investigation of a bistable piezoelectric inertial generator, Physica D 239 (2010) 640–653.

[16] L. V. Blarigan, P. Danzl, J. Moehlis, A broadband vibrational energy harvester, Applied Physics Letters 100 (2012) 253904.

[17] K. Ishida, T.-C. Huang, K. Honda, Y. Shinozuka, H. Fuketa, T. Yokota, U. Zschieschang, H. Klauk, G. Tortissier, T. Sekitani, H. Toshiyoshi, M. Takamiya, T. Someya, T. Sakurai, Insole pedometer with piezoelectric energy harvester and 2 V organic circuits, IEEE Journal of Solid-State Circuits 48 (2013) 255–264.

[18] Q. Tang, Y. Yang, X. Li, Repulsively driven frequency-increased-generators for durable energy harvesting from ultra-low frequency vibration, Reviews of Scientific Instruments 85 (2014) 045004.

[19] M. Bernitsas, K. Raghavan, Y. Ben-Simon, E. M. H. Garcia, Vivace (vortex induced vibration aquatic clean energy): A new concept in generation of clean and renewable energy from fluid flow, Journal of Offshore Mechanics and Arctic Engineering 130 (2008) 041101.

[20] D. Barton, S. Burrow, L. Clare, Energy harvesting from vibrations with a nonlinear oscillator, Journal of Vibration and Acoustics 132 (2010) 021009.

[21] W. Hobbs, D. Hu, Tree-inspired piezoelectric energy harvesting, Journal of Fluids and Structures.

[22] F. Moon, From Waves in Complex Systems to Dynamics of Generalized Continua, World Scientific, 2011, Ch. 15: Principles of vibro-wind energy conversion, pp. 385–401.

[23] M. Kubota, V. Putkaradze, T. Hikihara, Energy absorption at synchronization in phase between coupled duffing systems, International Journal of Dynamics and Control (2014) 2195–268X.

[24] S. McGarry, C. Knight, The potential for harvesting energy from the movement of trees, Sensors 11 (2011) 9275–9299.

[25] S. McGarry, C. Knight, Development and successful application of a tree movement energy harvesting device, to power a wireless sensor node, Sensors 12 (2012) 12110–12125.

[26] A. H. Nayfeh, B. Balachandran, Modal interactions in dynamical and structural systems, Applied Mechanics Reviews (1989) 175–201.

[27] L.-Q. Chen, W.-A. Jiang, Internal resonance energy harvesting, Journal of Applied Mechanics 82 (2015) 031004:1–14.

[28] O. M. O'Reilly, D. M. Peters, Nonlinear stability criteria for tree-like structures composed of branched elastic rods, Proceeding of Royal Society London A 468 (2012) 206–226.

[29] F. Hache, N. Challamel, I. Elishakoff, C. M. Wang, Comparison of non-local continualization schemes for lattice beams and plates, Arch. Appl Mech 87 (2017) 1105–1138.

[30] K. Murphy, M. Rudnicki, A physics-based link model for tree vibrations, American Journal of Botany 99 (2012) 1918–1929.

[31] F. Gay-Balmaz, D. D. Holm, V. Putkaradze, T. Ratiu, Exact geometric theory of dendronized polymer dynamics, Advances in Applied Mathematics 48 (2011) 535–574.

[32] L. D. Landau, E. M. Lifshitz, Course of theoretical physics, volume I: Mechanics, Pergamon Press, 1976.

[33] E. Bourguignon, M. R. Johnson, L. W. Kostiuk, The use of a closed-loop wind tunnel for measuring the combustion efficiency of flames in a cross flow, Combust. Flame 119 (1999) 319–334.

[34] T. J. Anderson, B. Balancandran, A. H. Nayfeh, Nonlinear resonances in a flexible cantilever beam, Transactions of the ASME 116 (1994) 480–484.

[35] S. Strogatz, From Kuramoto to Crawford: exploring the onset of synchronization in populations of coupled oscillators, Physica D 143 (2000) 1–20.

[36] R. W. Erickson, D. Maksimovic, Fundamentals of Power Electronics, 2nd Ed, Springer, 2007.

[37] C. Peters, J. Handwerker, D. Maurath, Y. Manoli, A sub-500 mv highly efficient active rectifier for energy harvesting applications, IEEE Transactions on Circuits and Systems (2011) 1542–1550.

[38] A. Stefanov, P. Kevrekidis, On the existence of solitary traveling waves for generalized Hertzian chains, Journal of Nonlinear Science 22 (2012) 327–349.

[39] M. Bagherinia, M. Bruggi, A. Corigliano, S. Mariani, E. Lasalandra, Geometry optimization of a Lorentz force, resonating MEMS magnetometer, Microelectronics Reliability 54 (2014) 1192–1199.

[40] M. Bagherinia, M. Bruggi, A. Corigliano, S. Mariani, D. A. Horsley, M. Li, E. Lasalandra, An efficient earth magnetic field mems sensor: Modeling, experimental results, and optimization, Journal of Microelectromechanical Systems 24 (2015) 887–895.

[41] T. Petropoulos, E. M. Yeatman, P. D. Mitcheson, MEMS coupled resonators for power generation and sensing, in: Proceedings of Micromechanics Europe, Leuven, Belgium, 2004, pp. 261–264.

[42] Z. Yang, J. Yang, Connected vibrating piezoelectric bimorph beams as a wide-band piezoelectric power harvester, Journal of Intelligent Material Systems and Structures 20 (2009) 569–574.

[43] A. Erturk, J. Hoffmann, D. J. Inman, A piezomagnetoelastic structure for broadband vibration energy harvesting, Applied Physics Letters 94 (2009) 254102.

[44] A. Erturk, J. Hoffmann, D. J. Inman, Modeling of piezoelectric energy harvesting from an l-shaped beam-mass structure with an application to uavs, Journal of Intelligent Material Systems and Structures 20 (2009) 529–544.

[45] C. Williams, R.B.Yates, Analysis of a micro-electric generator for microsystems, Sensors and Actuators A 52 (1996) 8–11.

[46] I. Sari, T. Balkan, H. Kulah, An electromagnetic micro power generator for wideband environmental vibrations, Sensors and Actuators A 145-146 (2008) 405–413.